

# **Accuracy of hybrid functionals with non-self-consistent Kohn-Sham orbitals for predicting the properties of semiconductors**

## **Electronic supporting information**

J. M. Skelton, D. S. D. Gunn, S. Metz and S. C. Parker

## S1. Convergence Testing

As discussed in the text, the plane-wave cutoffs and  $k$ -point sampling for each of the compounds tested were chosen in a manner representative of how these parameters would be chosen in a typical high-throughput modeling study. To check the parameters, we performed a series of explicit convergence tests with the PBE exchange-correlation functional<sup>1</sup> in which the base cutoffs in Table 1 in the text were increased by 1.5 and 2  $\times$  and the  $k$ -point sampling meshes were similarly increased to 1.5 and 2  $\times$  the base number of subdivisions along each reciprocal lattice vector.

Tables S1.1 and S1.2 show the convergence of the PBE bandgap  $E_g$  with respect to the cutoff and  $k$ -point sampling. Barring Ge, for which PBE with the base parameters predicts a near-metallic bandgap of 28 meV, these tests suggest the bandgaps are converged to within 1 % with the base cutoff. Similarly, with the exception of GaP, where a 1.4 % change in the gap is observed on increasing the  $k$ -point density, the tests suggest the base  $k$ -point meshes are sufficient to converge the calculated gaps to within 1 %.

Tables S1.3 and S1.4 show the convergence of the high-frequency dielectric constant  $\epsilon_\infty$  with respect to the cutoff and  $k$ -point sampling. As shown in Table S1.1, PBE predicts InAs and InSb to be metallic and Ge and GaSb to have very narrow gaps of < 100 meV respectively. We would therefore anticipate large variability in the calculated  $\epsilon_\infty$  for these compounds. With the exception of Ge, the tests indicate the calculated dielectric constants to be converged to < 1 % with respect to the cutoff. Excluding the four compounds identified above, the  $\epsilon_\infty$  of eight compounds are converged to < 1 % with respect to  $k$ -point sampling, the dielectric constants of a further three are converged to < 5 %, and the remaining compound, GaAs, is converged to 8.2 %.

Finally, Tables S1.5 and S1.6 show the convergence of the equilibrium total energies  $E_0$ , volumes  $V_0$  and bulk moduli  $B_0$  with respect to cutoff and  $k$ -point sampling. As described in the text, these parameters are obtained by fitting energy/volume curves to the Birch-Murnaghan equation of state (Eq. 1 in the text).<sup>2</sup> Our tests suggest that  $E_0$  and  $V_0$  are converged to well within 1 % with the base parameters.  $B_0$  is obtained from the curvature of the energy/volume curve and is thus more sensitive to small changes in the calculated energies. Nonetheless, our tests indicate that the  $B_0$  for nine of the sixteen compounds are converged to < 1 % with respect to the cutoff, a further five are converged to < 2.5 %, and the remaining two are converged to 2.72 and 5.75 %. The base cutoff was increased by 1.5  $\times$  for the production calculations presented in the text, and the  $B_0$  obtained with this cutoff are all converged to less than or around 1 % with respect to the higher 2  $\times$  plane-wave cutoff. The  $B_0$  appear to be more sensitive to the  $k$ -point sampling, but nonetheless the data in Table S1.6 suggests that for seven of the compounds the calculated  $B_0$  are converged to < 1 % with the base  $k$ -point meshes, a further four are converged to < 2.5 %, and the remainder are converged to < 5 %.

System	$E_g$ [eV]			Range [meV]	Std. [%]
	Base	1.5 ×	2 ×		
C	4.109	4.123	4.125	16.7	0.18
Si	0.591	0.585	0.584	7.0	0.53
Ge	0.028	0.031	0.031	3.1	5.24
AlP	1.569	1.568	1.568	1.3	0.04
AlAs	1.447	1.447	1.447	0.7	0.02
AlSb	1.216	1.215	1.215	0.9	0.03
GaP	1.637	1.636	1.636	1.5	0.04
GaAs	0.513	0.513	0.513	0.2	0.02
GaSb	0.093	0.094	0.094	1.1	0.48
InP	0.679	0.685	0.685	5.9	0.40
InAs	0.000	0.000	0.000	0.0	-
InSb	0.000	0.000	0.000	0.0	-
ZnS	2.098	2.102	2.103	5.1	0.10
ZnSe	1.285	1.286	1.287	1.6	0.05
ZnTe	1.245	1.246	1.247	2.2	0.07
CdTe	0.764	0.768	0.770	5.5	0.30

**Table S1.1** Convergence of the bandgap  $E_g$  with respect to plane-wave cutoff with the PBE exchange-correlation functional. The bandgaps obtained with the base cutoffs listed in Table 1 in the text and those calculated with the cutoffs increased by 1.5 and 2 × this value are shown together with the ranges of the three gaps in meV and the standard deviations as percentages of the gaps obtained with the base cutoffs.

System	$E_g$ [eV]			Range [meV]	Std. [%]
	Base	1.5 ×	2 ×		
C	4.109	4.116	4.109	7.5	0.09
Si	0.591	0.591	0.591	0.2	0.01
Ge	0.028	0.028	0.028	0.1	0.09
AlP	1.569	1.569	1.569	0.5	0.02
AlAs	1.447	1.448	1.448	0.7	0.02
AlSb	1.216	1.207	1.200	16.2	0.55
GaP	1.637	1.589	1.590	48.2	1.37
GaAs	0.513	0.514	0.514	0.8	0.07
GaSb	0.093	0.094	0.094	1.0	0.46
InP	0.679	0.680	0.680	0.6	0.04
InAs	0.000	0.000	0.000	0.0	-
InSb	0.000	0.000	0.000	0.0	-
ZnS	2.098	2.098	2.098	0.0	0.00
ZnSe	1.285	1.286	1.286	0.4	0.01
ZnTe	1.245	1.245	1.245	0.4	0.01
CdTe	0.764	0.765	0.765	0.5	0.03

**Table S1.2** Convergence of the bandgap  $E_g$  with respect to  $k$ -point sampling with the PBE exchange-correlation functional. The bandgaps obtained with the base  $k$ -point meshes listed in Table 1 in the text and values obtained using meshes increased by 1.5 and 2 × along each reciprocal lattice vector are shown together with the ranges of the three gaps in meV and the standard deviations as percentages of the gaps obtained with the base  $k$ -point meshes.

System	$\epsilon_{\infty}$			Range	Std. [%]
	Base	1.5 ×	2 ×		
C	5.88	5.88	5.87	$9.20 \times 10^{-3}$	0.07
Si	13.15	13.20	13.21	$5.47 \times 10^{-2}$	0.19
Ge	$2.03 \times 10^3$	$1.64 \times 10^3$	$1.64 \times 10^3$	-	-
AlP	8.62	8.64	8.64	$2.45 \times 10^{-2}$	0.13
AlAs	9.76	9.76	9.76	$3.60 \times 10^{-3}$	0.02
AlSb	12.19	12.19	12.19	$2.70 \times 10^{-3}$	0.01
GaP	10.90	10.91	10.91	$1.61 \times 10^{-2}$	0.07
GaAs	17.37	17.37	17.38	$3.90 \times 10^{-3}$	0.01
GaSb	$1.53 \times 10^2$	$1.51 \times 10^2$	$1.50 \times 10^2$	3.13	0.85
InP	12.17	12.16	12.15	$1.75 \times 10^{-2}$	0.06
InAs	17.62	17.70	17.69	$7.94 \times 10^{-2}$	0.20
InSb	21.56	21.66	21.70	0.14	0.28
ZnS	6.18	6.19	6.19	$1.19 \times 10^{-2}$	0.09
ZnSe	7.54	7.54	7.54	$3.60 \times 10^{-3}$	0.02
ZnTe	9.26	9.25	9.25	$5.40 \times 10^{-3}$	0.02
CdTe	9.21	9.19	9.18	$3.14 \times 10^{-2}$	0.14

**Table S1.3** Convergence of the high-frequency dielectric constant  $\epsilon_{\infty}$  with respect to plane-wave cutoff with the PBE exchange-correlation functional. The dielectric constants obtained with the base cutoffs listed in Table 1 in the text and values obtained with the cutoffs increased by 1.5 and 2 × are shown together with the ranges of the  $\epsilon_{\infty}$  and the standard deviations as percentages of the values obtained with the base cutoffs.

System	$\epsilon_{\infty}$			Range	Std. [%]
	Base	1.5 ×	2 ×		
C	5.88	5.92	5.93	$4.91 \times 10^{-2}$	0.35
Si	13.15	13.18	13.29	0.13	0.44
Ge	$2.03 \times 10^3$	$7.80 \times 10^2$	$4.24 \times 10^2$	-	-
AlP	8.62	8.59	8.65	$5.36 \times 10^{-2}$	0.26
AlAs	9.76	9.65	9.73	0.10	0.45
AlSb	12.19	11.85	11.91	0.34	1.22
GaP	10.90	10.67	10.73	0.23	0.89
GaAs	17.37	14.66	14.10	3.27	8.22
GaSb	$1.53 \times 10^2$	68.28	44.32	-	-
InP	12.17	11.35	11.25	0.92	3.39
InAs	17.62	15.65	15.48	-	-
InSb	21.56	18.59	18.15	-	-
ZnS	6.18	6.22	6.24	$6.36 \times 10^{-2}$	0.42
ZnSe	7.54	7.46	7.49	$8.56 \times 10^{-2}$	0.47
ZnTe	9.26	9.10	9.14	0.16	0.71
CdTe	9.21	8.87	8.85	0.36	1.80

**Table S1.4** Convergence of the high-frequency dielectric constant  $\epsilon_{\infty}$  with respect to  $k$ -point sampling with the PBE exchange-correlation functional. The dielectric constants obtained with the base  $k$ -point meshes listed in Table 1 in the text and  $\epsilon_{\infty}$  calculated using meshes increased by 1.5 and 2 × along each reciprocal lattice vector are shown together with the ranges of the  $\epsilon_{\infty}$  and the standard deviations as percentages of the values obtained with the base  $k$ -point meshes.

System	$E_0$ [eV]			Range [meV]	Std. [%]	$V_0$ [ $\text{\AA}^3$ ]			Range [ $10^{-3} \text{\AA}^3$ ]	Std. [%]	$B_0$ [GPa]			Range [GPa]	Std. [%]
	Base	1.5 $\times$	2 $\times$			Base	1.5 $\times$	2 $\times$			Base	1.5 $\times$	2 $\times$		
C	-18.21	-18.20	-18.21	13.0	-0.03	11.39	11.39	11.38	11.0	0.04	434.9	435.6	433.9	1.64	0.16
Si	-8.979	-8.994	-8.994	15.5	-0.08	48.31	48.16	48.15	154	0.15	55.14	56.80	56.72	1.65	1.38
Ge	-10.90	-10.92	-10.93	26.4	-0.11	40.79	40.68	40.67	116	0.13	88.39	89.51	89.55	1.16	0.61
AlP	-10.39	-10.40	-10.40	11.1	-0.05	41.65	41.55	41.55	94.4	0.11	83.58	83.27	83.18	0.39	0.20
AlAs	-9.395	-9.402	-9.403	7.8	-0.04	46.89	46.85	46.86	35.4	0.03	67.57	67.33	67.56	0.24	0.17
AlSb	-8.222	-8.226	-8.227	5.0	-0.03	60.30	60.26	60.25	44.7	0.03	49.59	49.74	49.84	0.25	0.21
GaP	-9.107	-9.114	-9.116	9.5	-0.04	41.72	41.68	41.67	43.0	0.05	76.18	75.96	76.42	0.46	0.25
GaAs	-8.237	-8.243	-8.246	9.4	-0.05	47.50	47.52	47.50	18.3	0.02	62.85	60.26	61.07	2.59	1.72
GaSb	-7.343	-7.347	-7.350	6.4	-0.04	60.09	60.09	60.09	5.74	0.00	41.75	41.78	41.55	0.24	0.25
InP	-8.401	-8.405	-8.406	4.8	-0.02	52.77	52.77	52.77	3.76	0.00	62.31	60.01	59.76	2.55	1.84
InAs	-7.690	-7.698	-7.697	7.5	-0.04	59.16	59.22	59.22	65.2	0.05	51.91	49.10	49.36	2.81	2.44
InSb	-6.932	-6.936	-6.939	6.9	-0.04	72.77	72.79	72.82	46.3	0.03	38.95	38.66	38.27	0.68	0.72
ZnS	-6.849	-6.856	-6.857	7.9	-0.05	40.38	40.33	40.32	58.7	0.07	68.26	69.14	69.53	1.28	0.78
ZnSe	-6.023	-6.025	-6.026	3.2	-0.02	47.20	47.18	47.19	16.0	0.01	55.02	56.77	56.78	1.76	1.50
ZnTe	-5.178	-5.181	-5.182	3.8	-0.03	59.01	58.94	58.95	73.8	0.06	41.23	43.75	43.44	2.52	2.72
CdTe	-4.786	-4.797	-4.802	16.3	-0.14	72.32	72.53	72.53	218	0.14	40.10	35.19	35.22	4.90	5.75

**Table S1.5** Convergence of the equilibrium total energies  $E_0$ , equilibrium volumes  $V_0$  and bulk moduli  $B_0$ , obtained by fitting energy/volume curves calculated with the PBE exchange-correlation functional to the Birch-Murnaghan equation of state (Eq. 6 in the text),<sup>2</sup> with respect to plane-wave cutoff. The parameters obtained with the base cutoffs listed in Table 1 in the text and those calculated with the cutoffs increased by 1.5 and 2  $\times$  this value are shown together with the ranges and the standard deviations as percentages of the values obtained with the base cutoffs. Note that the production calculations described in the text were performed with 1.5  $\times$  the base cutoffs.

System	$E_0$ [eV]			Range [meV]	Std. [%]	$V_0$ [Å <sup>3</sup> ]			Range [10 <sup>-3</sup> Å <sup>3</sup> ]	Std. [%]	$B_0$ [GPa]			Range [GPa]	Std. [%]
	Default	1.5 ×	2 ×			Default	1.5 ×	2 ×			Default	1.5 ×	2 ×		
C	-18.21	-18.21	-18.21	0.0	0.00	11.39	11.39	11.38	0.69	0.00	434.9	432.9	432.9	2.08	0.22
Si	-10.90	-10.90	-10.90	0.8	0.00	40.79	40.79	40.79	0.88	0.00	88.39	88.53	88.49	0.14	0.07
Ge	-8.979	-8.989	-8.989	10.6	-0.05	48.31	48.27	48.18	129	0.11	55.14	55.93	60.27	5.12	4.08
AlP	-10.39	-10.39	-10.39	0.9	0.00	41.65	41.64	41.64	8.06	0.01	83.58	83.48	83.32	0.26	0.13
AlAs	-9.395	-9.397	-9.397	1.7	-0.01	46.89	46.89	46.89	5.26	0.00	67.57	66.85	66.89	0.72	0.49
AlSb	-8.222	-8.225	-8.225	2.6	-0.01	60.30	60.30	60.30	3.44	0.00	49.59	49.93	49.84	0.34	0.29
GaP	-9.107	-9.109	-9.109	2.6	-0.01	41.72	41.71	41.72	9.79	0.01	76.18	76.83	76.29	0.66	0.37
GaAs	-8.237	-8.242	-8.242	5.7	-0.03	47.50	47.57	47.58	76.9	0.07	62.85	60.12	59.75	3.10	2.20
GaSb	-7.343	-7.349	-7.350	7.0	-0.04	60.09	59.96	60.00	133	0.09	41.75	45.48	43.91	3.74	3.67
InP	-8.401	-8.404	-8.404	2.4	-0.01	52.77	52.81	52.81	45.3	0.04	62.31	59.70	59.77	2.61	1.95
InAs	-7.690	-7.694	-7.694	4.1	-0.02	59.16	59.22	59.23	73.4	0.06	51.91	49.24	48.87	3.04	2.61
InSb	-6.932	-6.937	-6.937	5.6	-0.04	72.77	72.81	72.90	132	0.08	38.95	37.65	36.26	2.69	2.82
ZnS	-6.849	-6.849	-6.849	0.2	0.00	40.38	40.37	40.38	9.21	0.01	68.26	69.18	68.53	0.92	0.57
ZnSe	-6.023	-6.024	-6.023	0.9	-0.01	47.20	47.20	47.20	0.74	0.00	55.02	56.87	56.23	1.85	1.39
ZnTe	-5.178	-5.180	-5.180	1.2	-0.01	59.01	58.96	58.96	50.0	0.04	41.23	43.09	43.18	1.95	2.18
CdTe	-4.786	-4.788	-4.787	1.9	-0.02	72.32	72.57	72.49	253	0.15	40.10	35.32	36.93	4.78	4.95

**Table S1.6** Convergence of the equilibrium total energies  $E_0$ , equilibrium volumes  $V_0$  and bulk moduli  $B_0$ , obtained by fitting energy/volume curves calculated with the PBE exchange-correlation functional to the Birch-Murnaghan equation of state (Eq. 6 in the text),<sup>2</sup> with respect to  $k$ -point sampling. The parameters obtained with the base  $k$ -point sampling listed in Table 1 in the text and those calculated with the meshes increased by 1.5 and 2 × along each of the reciprocal lattice vectors this value are shown together with the ranges and the standard deviations as percentages of the values obtained with the base  $k$ -point meshes.



## S2. Calculation of High-Frequency Dielectric Constants

In this section we discuss the calculation of the high-frequency dielectric constant  $\epsilon_\infty$  and compare the values obtained using the independent-particle random-phase approximation (IP-RPA) method employed for the calculations in the text to those obtained using density-functional perturbation theory (DFPT) and from the self-consistent response to finite fields.

VASP implements several methods of calculating  $\epsilon_\infty$  viz. using the IP-RPA (the `LOPTICS` tag), using DFPT (`LEPSILON`),<sup>3</sup> and from the response to a finite electric field (`LCALCEPS`).<sup>4</sup> All three methods are available for use with the LDA and GGA functionals, whereas DFPT is not implemented for meta-GGA and non-local hybrid functionals. More sophisticated methods of evaluating the dielectric properties are also available, including time-dependent density-functional theory (TD-DFT), *GW* theory and the Bethe-Salpeter equation (BSE),<sup>5-7</sup> but we consider the present implementations to be too computationally demanding for high-throughput modeling and therefore beyond the scope of this work.

$\epsilon_\infty$  is obtained in the IP-RPA formalism from the frequency-dependent dielectric function  $\epsilon(E) = \epsilon_{\text{re}}(E) + i\epsilon_{\text{im}}(E)$  as  $\epsilon_\infty = \epsilon_{\text{re}}(E = 0)$ . The imaginary part of the dielectric function  $\epsilon_{\text{im}}(E)$  is evaluated as a weighted sum of transitions between occupied and virtual states using Fermi's Golden Rule, and the real part  $\epsilon_{\text{re}}(E)$  is then obtained from the Kramers-Kronig relation. This method requires a significant number of empty conduction states to be included in the calculation in order to converge, and the VASP implementation also neglects local-field effects. The DFPT and finite-field approaches do not require additional virtual states to be included in calculations. The DFPT implementation calculates  $\epsilon_\infty$  both with and without local-field effects, while the finite-field method includes local-field effects implicitly. However, DFPT and the finite-field method both involve iterative processes that are incompatible with non-self-consistent calculations.

To compare the accuracy of the different approaches, we computed the dielectric constants of the sixteen semiconductors in Table 1 in the text using PBE<sup>1</sup> with the DFPT, finite-field and IP-RPA methods, and using PBE0<sup>8</sup> and HSE06<sup>9</sup> with the finite-field and IP-RPA methods (Table S2.1).

Comparing the PBE DFPT calculations with and without local-field effects shows that these effects reduce  $\epsilon_\infty$  by an average 4.05 %. DFPT predicts anomalously-large dielectric constants for Ge and GaSb, which we attribute to the small but finite PBE bandgaps of 28 and 93 meV (see text). The metallic electronic structures of InAs and InSb result in  $\epsilon_\infty$  being overestimated by  $1.2\text{-}3.7 \times$  the experimental values, although these results are far more realistic than those for Ge and GaSb.

The finite-field method is prone to failure in narrow-gap systems due to interband (Zener) tunnelling.<sup>10</sup> The  $\epsilon_\infty$  obtained for Ge, GaSb, InAs and InSb using this method are all significantly overestimated at  $1.4\text{-}9.6 \times$  the experimental values, although the method does not diverge for Ge and GaSb as DFPT does. Excluding

these four systems, the  $\epsilon_{\infty}$  obtained from the finite-field and IP-RPA methods are an average 13 and 10.7 % smaller than the equivalent DFPT values. Particularly large differences are observed for GaAs, InP and CdTe, and further excluding these data points reduces the average differences to 5.68 and 5.43 %. In principle, the IP-RPA and DFPT results excluding local-field effects should match, but given the clearly anomalous results obtained for some compounds with DFPT the origin of the discrepancy is not clear.

To verify the convergence of the IP-RPA results with respect to the number of virtual states, we compared the  $\epsilon_{\infty}$  obtained with our chosen number of virtual states (see text) to those calculated using orbital energies from exact diagonalization of the Hamiltonian in the full basis spanned by the plane-wave cutoff, ranging from 216 bands for diamond (a  $54 \times$  excess of virtual states) to 725 for CdTe ( $\sim 80 \times$  excess; Table S2.2). The two sets of results are well within 1 % of each other, indicating that the IP-RPA calculations are converged and an insufficient number of unoccupied states is unlikely to explain the discrepancy between the DFPT and IP-RPA results.

In the finite-field calculations, we found that the  $\epsilon_{\infty}$  converge much more slowly than the total energy. By default, the convergence criteria are tightened by two orders of magnitude during the field-polarised calculations, so that our chosen tolerance of  $10^{-6}$  eV on the total energy implies a tolerance of  $10^{-8}$  eV under the applied field. To check convergence with respect to the tolerance, we performed a further set of calculations with a tighter  $10^{-8}$  eV tolerance (i.e.  $10^{-10}$  eV under the field). As shown in Table S2.2, this tighter tolerance is necessary to converge the calculated  $\epsilon_{\infty}$  to  $< 0.1$ , and is particularly important for the small-gap systems. We therefore used the tighter  $10^{-8}$  eV tolerance during all our finite-field calculations.

Returning to the data in Table S2.1, using PBE0 with the IP-RPA method underestimates the  $\epsilon_{\infty}$  obtained with the finite-field method by an average 21.3 %. For HSE06 the average difference is a much smaller 3.2 %, although a general tendency to underestimate is masked by large overestimates for InAs and InSb, without which the average underestimation rises to 5.6 %. The finite-field values are consistently closer to the experimental measurements (Table S2.3; c.f. Table 1 in the text and Table S2.1), with mean average relative errors (MAREs; Eq. 2 in the text) of  $7.16 \pm 5.76$  and  $5.56 \pm 4.74$  % for PBE0 and HSE06, respectively, compared to errors of  $26.8 \pm 7.04$  and  $9.13 \pm 2.89$  % using the IP-RPA method. With the exception of the PBE0 IP-RPA results, the dielectric constants predicted by the hybrid functionals are closer to the experimental measurements than the three sets of values predicted with PBE, although excluding the four zero/small-gap compounds the PBE finite-field calculations show good performance, with a MARE OF  $12.8 \pm 4.82$  %.

The accuracy with which  $\epsilon_{\infty}$  can be calculated is important for the dielectric-dependent scPBE0 calculations. Table S2.4 compares the optimised exact-exchange fractions  $\alpha$ , bandgaps and dielectric constants obtained using the IPA-RPA and finite-field approaches to calculate  $\epsilon_{\infty}$ . The narrow bandgaps of InSb and InAs made the finite-field calculations unstable after the initial self-consistent updates of  $\alpha$ , so these

systems were excluded from testing. These two compounds, together with Ge and GaSb, were similarly excluded from the scPBE0 calculations using the IP-RPA method due to the divergence of  $\epsilon_\infty$  as  $\alpha \rightarrow 0$ .

Across the 12 systems included in both calculations, the IP-RPA overestimates  $\alpha$  by an average 13 % compared to the finite-field values, leading to differences in the converged bandgaps and high-frequency dielectric constants of 4.9 and -11.4 % respectively (Table S2.4). The  $\epsilon_\infty$  obtained from the finite-field scPBE0 calculations are generally a better match to experiment, with a smaller MARE of  $4.73 \pm 4.38$  % compared to  $9.65 \pm 2.71$  % (Table S2.3). Both sets of results are however a significant improvement over bare PBE0 and are comparable to the HSE06 calculations, with a slightly smaller MARE for the finite-field scPBE0 results and a slightly larger one for the corresponding IP-RPA values.

System	PBE				HSE06		PBE0	
	DFPT <sup>a</sup>	DFPT <sup>b</sup>	Finite Field	IP-RPA	Finite Field	IP-RPA	Finite Field	IP-RPA
C	5.96	5.85	5.84	5.88	5.61	5.08	5.59	4.72
Si	13.89	13.27	12.80	13.15	11.11	10.04	10.86	8.23
Ge	$1.00 \times 10^5$	$9.30 \times 10^4$	24.35	$2.02 \times 10^3$	14.75	15.81	14.28	10.95
AlP	8.96	8.32	8.06	8.62	7.22	6.91	7.14	5.86
AlAs	10.36	9.78	9.18	9.76	8.11	7.63	8.00	6.37
AlSb	13.22	12.66	11.36	12.19	9.65	9.02	9.46	7.25
GaP	11.75	11.21	10.20	10.90	9.65	8.20	8.70	6.80
GaAs	29.99	29.57	13.14	17.37	10.50	9.99	10.31	7.89
GaSb	$2.01 \times 10^3$	$1.98 \times 10^3$	20.69	$1.53 \times 10^2$	12.89	12.92	12.47	9.39
InP	15.63	15.22	10.67	12.17	8.85	8.24	8.68	6.67
InAs	15.71	15.18	24.09	17.61	11.47	13.25	10.93	8.32
InSb	57.95	56.66	150.71	21.56	12.75	14.29	12.15	9.10
ZnS	6.31	5.93	5.90	6.18	5.12	4.89	5.09	4.38
ZnSe	8.15	7.78	7.11	7.54	5.95	5.60	5.91	4.85
ZnTe	10.05	9.62	8.71	9.26	7.31	6.85	7.22	5.75
CdTe	10.84	10.47	8.47	9.21	6.99	6.52	6.88	5.42

**Table S2.1** High-frequency dielectric constants  $\epsilon_\infty$  for the sixteen tetrahedral semiconductors in Table 1 in the text calculated with PBE, PBE0 and HSE06 using the density-functional theory (DFPT), finite-field and independent-particle random-phase approximation (IP-RPA) summation methods. <sup>a</sup> DFPT values excluding local-field effects. <sup>b</sup> DFPT values including local-field effects.

System	IP-RPA	IP-RPA (Exact)	Finite Field ( $10^{-6}$ )	Finite Field ( $10^{-8}$ )
C	5.88	5.87	5.46	5.84
Si	13.15	13.16	12.66	12.80
Ge	$2.02 \times 10^3$	$2.02 \times 10^3$	17.74	24.35
AlP	8.62	8.62	8.16	8.06
AlAs	9.76	9.75	9.32	9.18
AlSb	12.19	12.20	11.44	11.36
GaP	10.90	10.91	9.99	10.20
GaAs	17.37	17.39	12.31	13.14
GaSb	152.6	152.7	16.66	20.69
InP	12.17	12.20	10.16	10.67
InAs	17.61	17.64	23.10	24.09
InSb	21.56	21.64	131.9	150.7
ZnS	6.18	6.19	5.82	5.90
ZnSe	7.54	7.55	6.98	7.11
ZnTe	9.26	9.28	8.63	8.71
CdTe	9.21	9.27	8.22	8.47

**Table S2.2** Comparison of high-frequency dielectric constants  $\epsilon_\infty$  calculated using PBE with the independent-particle random-phase approximation (IP-RPA) and finite-field methods. The second and third columns compare values obtained from IP-RPA calculations using the numbers of virtual states listed in the text and with the virtual states obtained by exact diagonalization of the Hamiltonian in the full orbital basis spanned by the plane-wave cutoff. The fourth and fifth columns compare finite-field results obtained with tolerances of  $10^{-6}$  and  $10^{-8}$  eV on the total energy during the initial electronic-structure optimisation, which correspond to tighter tolerances of  $10^{-8}$  and  $10^{-10}$  eV in the subsequent field-polarised calculations.

XC Functional	Method	MAE	MARE [%]
PBE <sup>a</sup>	DFPT <sup>b</sup>	$3.86 \pm 4.79$	$42.4 \pm 42.6$
	DFPT <sup>c</sup>	$3.41 \pm 4.80$	$36.8 \pm 43.2$
	Finite Field	$0.89 \pm 0.34$	$12.8 \pm 4.82$
	IP-RPA	$1.95 \pm 1.48$	$22.7 \pm 12.9$
HSE06	Finite Field	$0.69 \pm 0.91$	$5.56 \pm 4.74$
	IP-RPA	$0.91 \pm 0.43$	$9.13 \pm 2.89$
PBE0	Finite Field	$0.88 \pm 0.95$	$7.16 \pm 5.76$
	IP-RPA	$2.86 \pm 1.67$	$26.8 \pm 7.04$
scPBE0 <sup>d</sup>	Finite Field	$0.54 \pm 0.76$	$4.73 \pm 4.38$
	IP-RPA	$0.76 \pm 0.17$	$9.65 \pm 2.71$
scPBE0 (PBE) <sup>e</sup>	IP-RPA	$0.90 \pm 0.19$	$11.6 \pm 3.71$

**Table S2.3** Comparison of the mean absolute error (MAE; Eq. 1 in the text) and mean absolute relative error (MARE; Eq. 2 in the text) in the high-frequency dielectric constants  $\epsilon_\infty$  of the sixteen tetrahedral semiconductors in Table 1 in the text calculated using the different approaches described above. <sup>a</sup> The PBE results exclude InP, InAs, Ge and GaSb due to the zero or very narrow PBE bandgaps and resultant large error in the calculated  $\epsilon_\infty$  (see above for explanation). <sup>b</sup> DFPT values excluding local-field effects. <sup>c</sup> DFPT values including local-field effects. <sup>d</sup> scPBE0 finite-field results exclude InSb and InAs as the narrow bandgaps caused the finite-field calculations to become unstable after the initial self-consistent updates of  $\alpha$  (see text). <sup>e</sup> These results exclude InP, InAs, Ge and GaSb due to the divergence of  $\epsilon_\infty$  as  $\alpha \rightarrow 0$  (see text).

System	Finite Field			Summation (IPA)		
	$\alpha$	$E_g$ [eV]	$\epsilon_\infty$	$\alpha$	$E_g$ [eV]	$\epsilon_\infty$
C	0.177	5.45	5.66	0.203	5.65	4.92
Si	0.083	0.98	12.06	0.093	1.03	10.79
Ge	0.053	0.29	18.97	-	-	-
AlP	0.133	2.29	7.52	0.149	2.38	6.72
AlAs	0.117	2.04	8.56	0.131	2.11	7.63
AlSb	0.095	1.66	10.56	0.105	1.71	9.52
GaP	0.106	2.19	9.47	0.118	2.26	8.48
GaAs <sup>a</sup>	0.084	0.98	11.92	0.086	0.99	11.63
GaSb	0.062	0.40	16.24	-	-	-
InP	0.104	1.23	9.64	0.116	1.29	8.62
InAs	-	-	-	-	-	-
InSb	-	-	-	-	-	-
ZnS	0.191	3.51	5.24	0.221	3.74	4.52
ZnSe	0.160	2.38	6.26	0.189	2.58	5.28
ZnTe	0.128	1.99	7.84	0.148	2.11	6.78
CdTe	0.134	1.47	7.48	0.159	1.61	6.30

**Table S2.4** Comparison of the optimised fraction of exact exchange  $\alpha$ , bandgap  $E_g$  and high-frequency dielectric constants  $\epsilon_\infty$  for the sixteen semiconductors in Table 1 in the text obtained from scPBEO calculations using the finite-field and independent-particle random-phase approximation (IP-RPA) methods. <sup>a</sup> Using the finite-field method, it was not possible to converge  $\epsilon_\infty$  to  $< 10^{-2}$ , even with the tighter optimisation tolerance of  $10^{-8}$  eV (see text); this value is therefore the average of the last six optimisation cycles during which  $\alpha$  stabilised to a value of 0.084.

### S3. Calculated Bandgaps

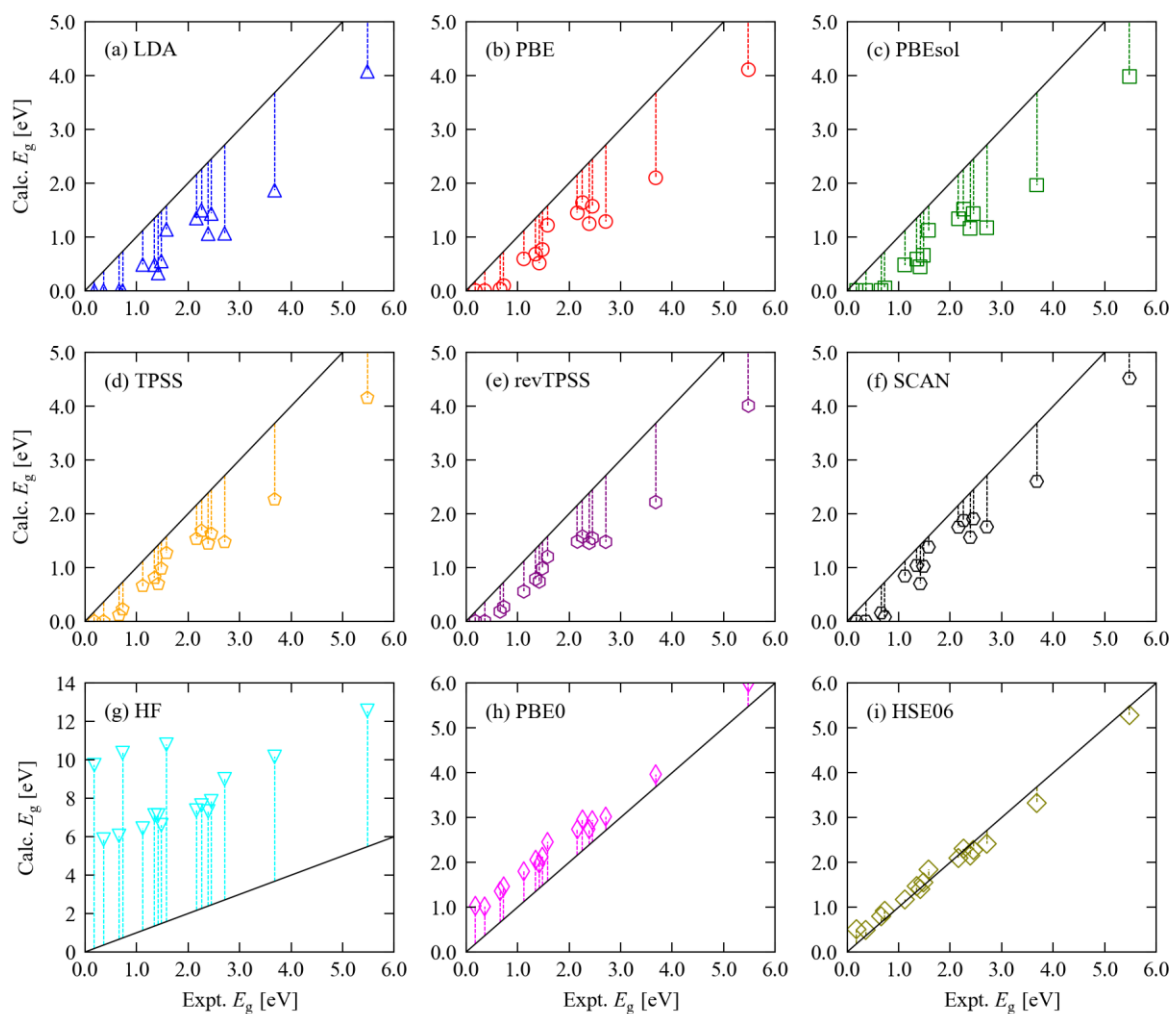


**Figure S3.1** Comparison of the experimental bandgaps  $E_g$  of the sixteen tetrahedral semiconductors examined in this work to bandgaps calculated with the LDA (a),<sup>11</sup> the PBE (b)<sup>1</sup> and PBEsol (c)<sup>12</sup> GGA functionals, the TPSS (d),<sup>13</sup> revTPSS (e)<sup>14</sup> and SCAN (f)<sup>15</sup> meta-GGA functionals, Hartree-Fock (g) and the PBE0 (h)<sup>8</sup> and HSE06 (i)<sup>9</sup> hybrid functionals.



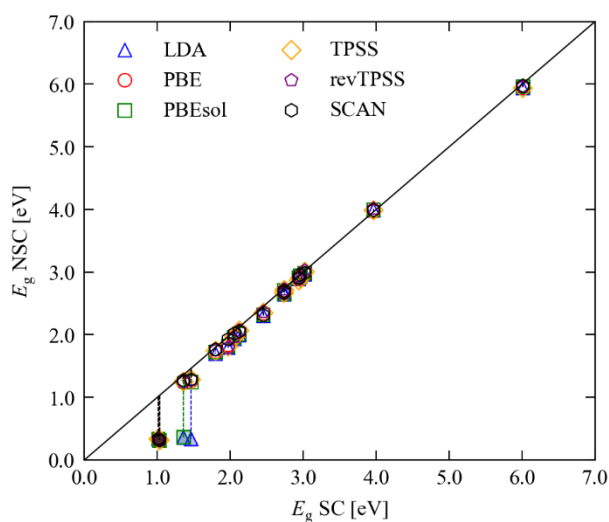


**Figure S3.2** Comparison of the self-consistent (SC) PBE0 bandgaps to non-self-consistent (NSC) PBE0 gaps calculated with orbitals from LDA (blue triangles), PBE (red circles), PBEsol (green squares), TPSS (orange diamonds), revTPSS (purple pentagons) and SCAN (black hexagons). Shaded markers denote systems for which the base functional predicts a bandgap of < 10 meV.

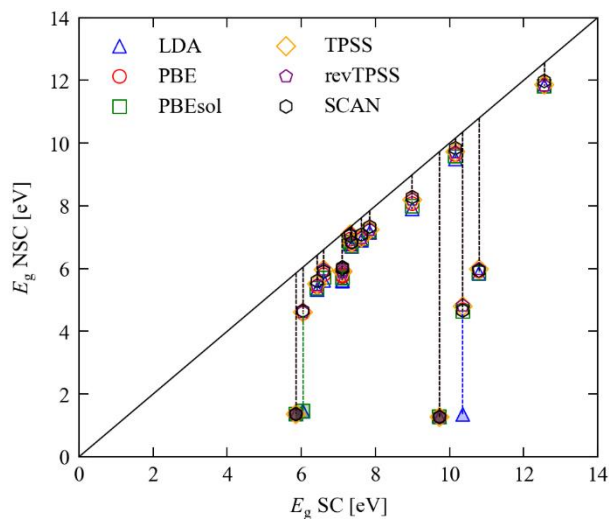


**Figure S3.3** Comparison of the self-consistent (SC) Hartree-Fock bandgaps to non-self-consistent (NSC) HF gaps calculated with orbitals from LDA (blue triangles), PBE (red circles), PBEsol (green squares), TPSS (orange diamonds), revTPSS (purple pentagons) and SCAN (black hexagons). Shaded markers denote systems for which the base functional predicts a bandgap of < 10 meV.

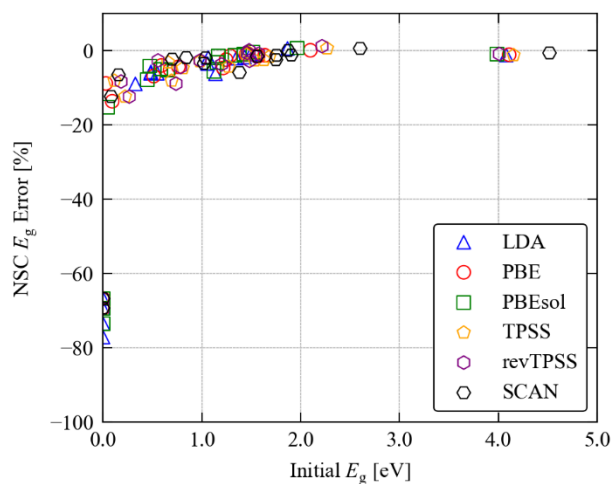


**Figure S3.4** Percentage error on non-self-consistent PBE0 bandgaps calculated using wavefunctions from the LDA, PBE and PBEsol GGA and TPSS, revTPSS and SCAN meta-GGA functionals as a function of the bandgap predicted by the base functional.

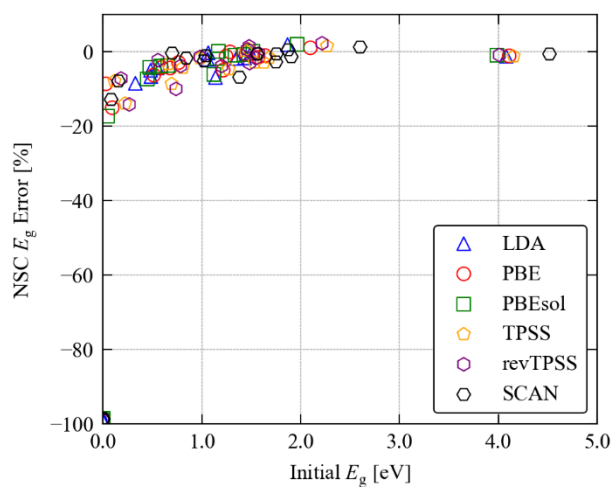


**Figure S3.5** Percentage error on non-self-consistent HSE06 bandgaps calculated using orbitals from the LDA, PBE and PBEsol GGA and TPSS, revTPSS and SCAN meta-GGA functionals as a function of the bandgap predicted by the base functional.

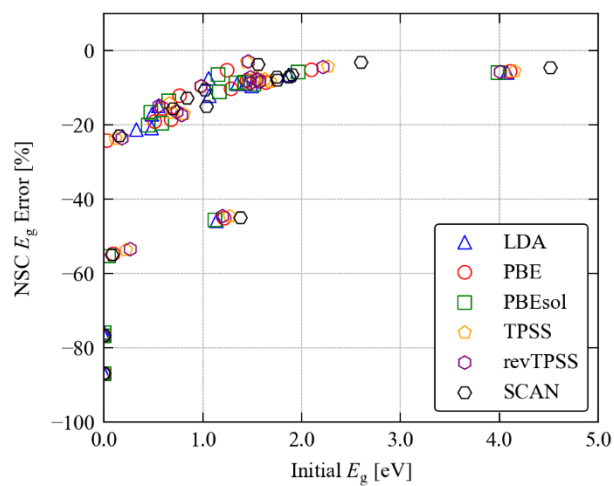


**Figure S3.6** Percentage error on non-self-consistent Hartree-Fock bandgaps calculated using orbitals from the LDA, PBE and PBEsol GGA and TPSS, revTPSS and SCAN meta-GGA functionals as a function of the bandgap predicted by the base functional.

#### S4. Density of States, Band Dispersions and Dielectric Properties

System	PBE			HSE06 (PBE)			HSE06		
	$E_F$ [eV]	$E_{VBM}$ [eV]	$E_{CBM}$ [eV]	$E_F$ [eV]	$E_{VBM}$ [eV]	$E_{CBM}$ [eV]	$E_F$ [eV]	$E_{VBM}$ [eV]	$E_{CBM}$ [eV]
C	9.973	9.969	14.08	9.423	9.418	14.64	9.347	9.339	14.62
Si	5.928	5.929	6.511	5.607	5.603	6.715	5.571	5.566	6.727
Ge	4.067	4.068	4.096	3.761	3.756	4.484	3.696	3.691	4.487
AlP	4.664	4.663	6.232	4.194	4.190	6.432	4.173	4.173	6.449
AlAs	3.207	3.198	4.646	2.750	2.743	4.826	2.761	2.754	4.850
AlSb	4.892	4.889	6.089	4.527	4.525	6.255	4.448	4.447	6.264
GaP	4.733	4.727	6.314	4.287	4.280	6.523	4.282	4.279	6.552
GaAs <sup>a</sup>	3.290	3.287	3.800	2.862	2.860	4.176	2.889	2.882	4.286
GaSb	5.089	5.087	5.181	4.751	4.750	5.529	4.681	4.676	5.594
InP	5.205	5.199	5.879	4.787	4.782	6.189	4.769	4.768	6.238
InAs	3.920	3.919	3.919	3.699	3.516	3.516	3.538	3.525	4.016
InSb	5.187	5.188	5.188	5.017	4.853	4.853	4.783	4.779	5.286
ZnS	2.162	2.156	4.254	1.301	1.296	4.656	1.424	1.423	4.747
ZnSe	1.806	1.805	3.090	1.049	1.041	3.454	1.150	1.142	3.556
ZnTe	3.318	3.315	4.560	2.737	2.732	4.858	2.779	2.773	4.924
CdTe	2.456	2.450	3.214	1.933	1.926	3.433	1.932	1.930	3.482

**Table S4.1** Fermi energies  $E_F$  and energies of the valence-band minima and conduction-band maxima ( $E_{VBM}/E_{CBM}$ ) obtained with PBE,<sup>1</sup> non-self-consistent HSE06 using the PBE orbitals, and self-consistent HSE06.<sup>9</sup> The  $E_F$  are obtained from the calculation used to generate the DoS in Figs. S4.1 - S4.16, and the  $E_{VBM}$  and  $E_{CBM}$  are obtained along the  $k$ -point path in the dispersion curves.

System	PBE			HSE06 (PBE)		
	$\Delta E_F$ [meV]	$\Delta E_{VBM}$ [meV]	$\Delta E_{CBM}$ [meV]	$\Delta E_F$ [meV]	$\Delta E_{VBM}$ [meV]	$\Delta E_{CBM}$ [meV]
C	626	631	-539	75.9	79.1	20.5
Si	357	363	-217	35.5	37.2	-12.2
Ge	371	377	-392	65.0	65.1	-3.6
AlP	492	491	-217	21.6	16.8	-17.0
AlAs	446	445	-204	-11.4	-10.2	-23.0
AlSb	444	442	-175	79.3	78.0	-9.0
GaP	452	448	-238	5.1	1.0	-29.4
GaAs <sup>a</sup>	401	405	-486	-26.4	-22.3	-110
GaSb	407	411	-413	69.7	73.4	-64.6
InP	436	432	-359	17.8	14.9	-49.1
InAs	381	394	-97.0	-	-	-
InSb	405	409	-98.4	-	-	-
ZnS	738	733	-493	-123	-127	-91.1
ZnSe	656	663	-466	-102	-101	-102
ZnTe	539	542	-364	-41.7	-41.1	-66.4
CdTe	524	520	-268	0.9	-3.4	-48.4
Average [meV]	524	520	-268	0.9	-3.4	-48.4
Std. Dev [meV]	107	106	139	60.3	61.1	38.1

**Table S4.2** Differences in the Fermi energies  $E_F$  and energies of the valence-band minima and conduction-band maxima ( $E_{VBM}/E_{CBM}$ ) obtained with PBE and non-self-consistent HSE06 to fully-self-consistent HSE06 calculations. The average and standard deviation (std. dev.) of the values in each column are given in the bottom two rows of the table.

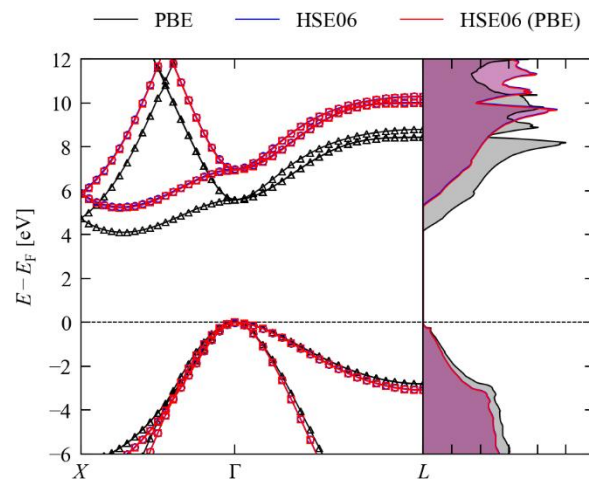


**Figure S4.1** Comparison of the electronic band dispersion and density of states  $g(E)$  for C calculated using PBE (black), HSE06 (blue) and non-self-consistent HSE06 calculations using the PBE orbitals (red).

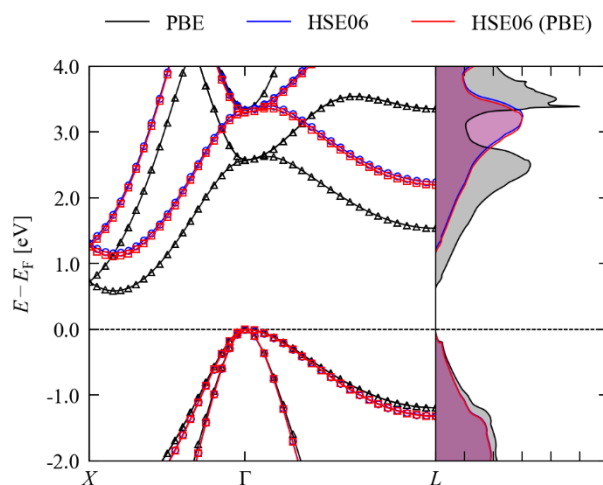


**Figure S4.2** Comparison of the electronic band dispersion and density of states  $g(E)$  for Si calculated using PBE (black), HSE06 (blue) and non-self-consistent HSE06 calculations using the PBE orbitals (red).

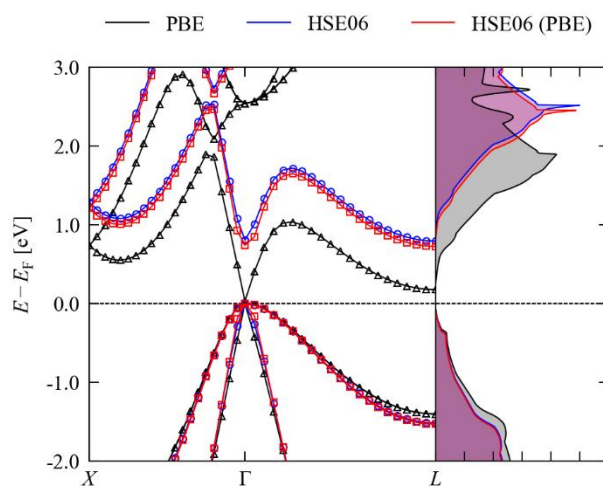


**Figure S4.3** Comparison of the electronic band dispersion and density of states  $g(E)$  for Ge calculated using PBE (black), HSE06 (blue) and non-self-consistent HSE06 calculations using the PBE orbitals (red).

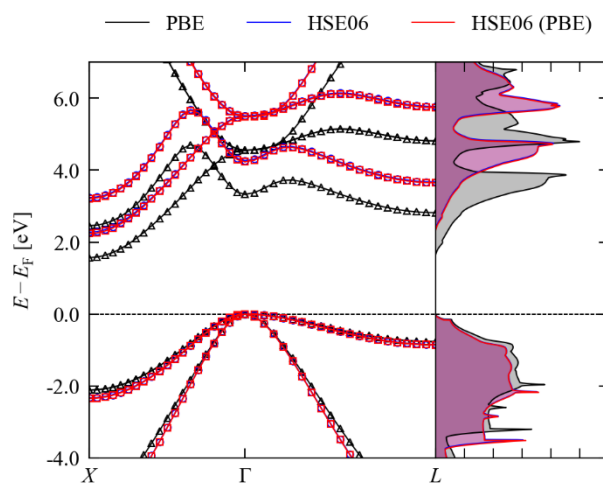


**Figure S4.4** Comparison of the electronic band dispersion and density of states  $g(E)$  for AlP calculated using PBE (black), HSE06 (blue) and non-self-consistent HSE06 calculations using the PBE orbitals (red).

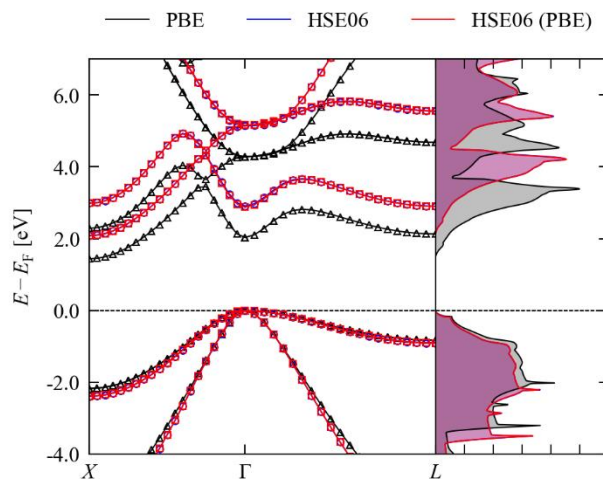


**Figure S4.5** Comparison of the electronic band dispersion and density of states  $g(E)$  for AlAs calculated using PBE (black), HSE06 (blue) and non-self-consistent HSE06 calculations using the PBE orbitals (red).

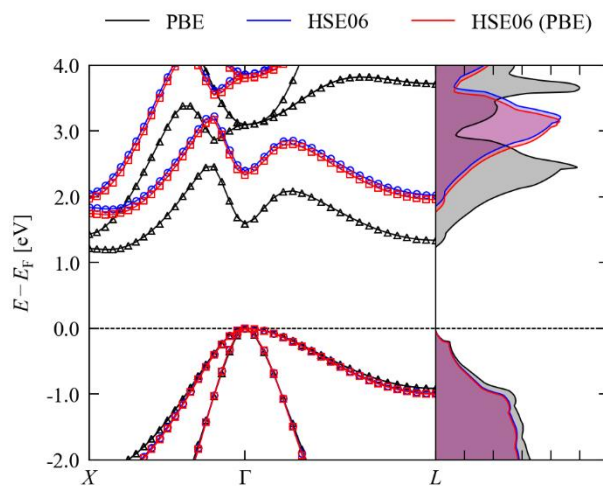


**Figure S4.6** Comparison of the electronic band dispersion and density of states  $g(E)$  for AlSb calculated using PBE (black), HSE06 (blue) and non-self-consistent HSE06 calculations using the PBE orbitals (red).



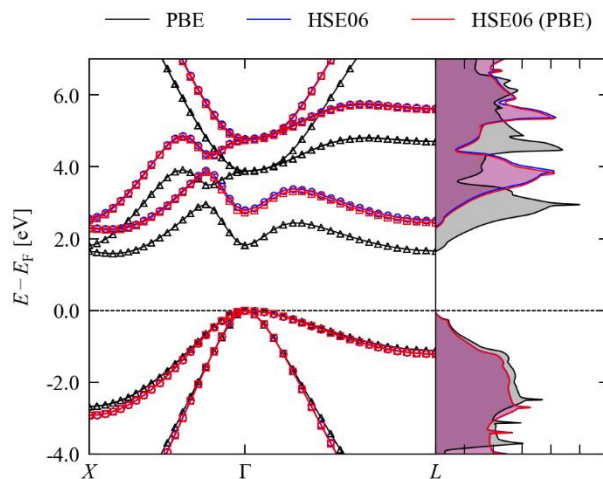


**Figure S4.7** Comparison of the electronic band dispersion and density of states  $g(E)$  for GaP calculated using PBE (black), HSE06 (blue) and non-self-consistent HSE06 calculations using the PBE orbitals (red).

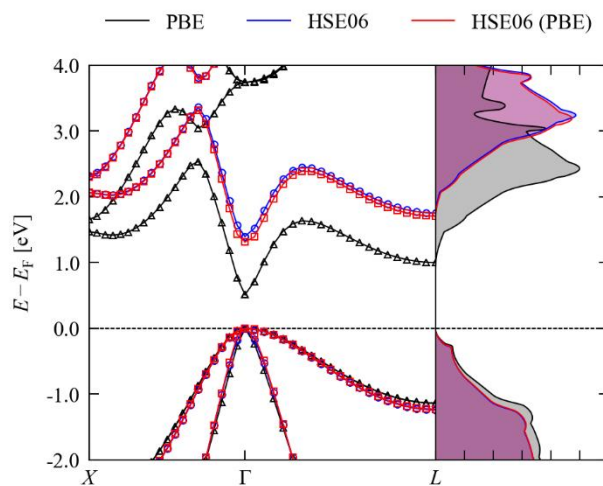


**Figure S4.8** Comparison of the electronic band dispersion and density of states  $g(E)$  for GaAs calculated using PBE (black), HSE06 (blue) and non-self-consistent HSE06 calculations using the PBE orbitals (red).

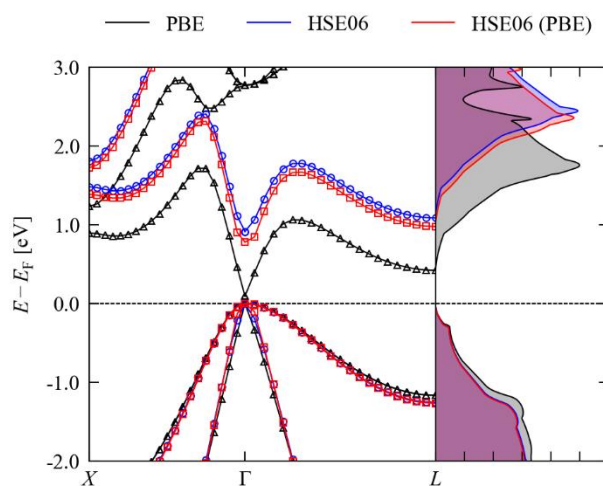


**Figure S4.9** Comparison of the electronic band dispersion and density of states  $g(E)$  for GaSb calculated using PBE (black), HSE06 (blue) and non-self-consistent HSE06 calculations using the PBE orbitals (red).

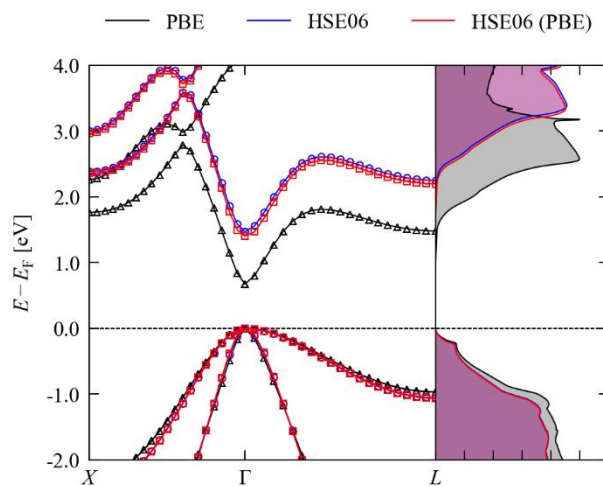


**Figure S4.10** Comparison of the electronic band dispersion and density of states  $g(E)$  for InP calculated using PBE (black), HSE06 (blue) and non-self-consistent HSE06 calculations using the PBE orbitals (red).

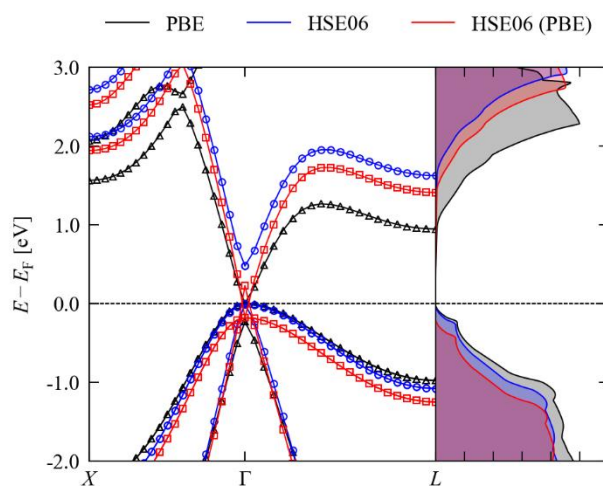


**Figure S4.11** Electronic band dispersion and density of states  $g(E)$  for InAs calculated using PBE (black), HSE06 (blue) and non-self-consistent HSE06 calculations using the PBE orbitals (red). The PBE functional predicts a metallic electronic structure for this compound, resulting in notably larger errors in the non-self-consistent calculations (see text).

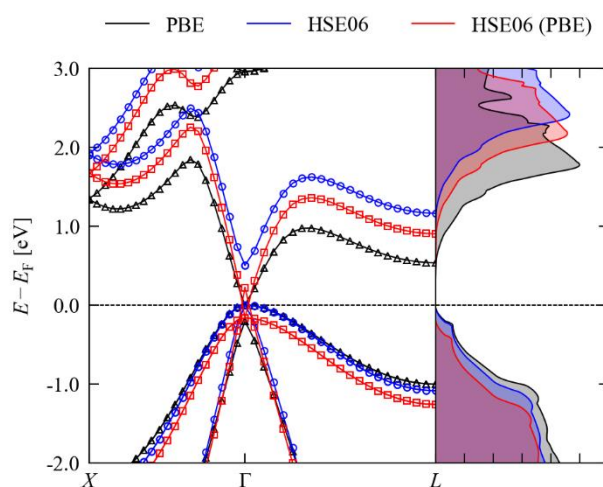


**Figure S4.12** Electronic band dispersion and density of states  $g(E)$  for InSb calculated using PBE (black), HSE06 (blue) and non-self-consistent HSE06 calculations using the PBE orbitals (red). The PBE functional predicts a metallic electronic structure for this compound, resulting in notably larger errors in the non-self-consistent calculations (see text).

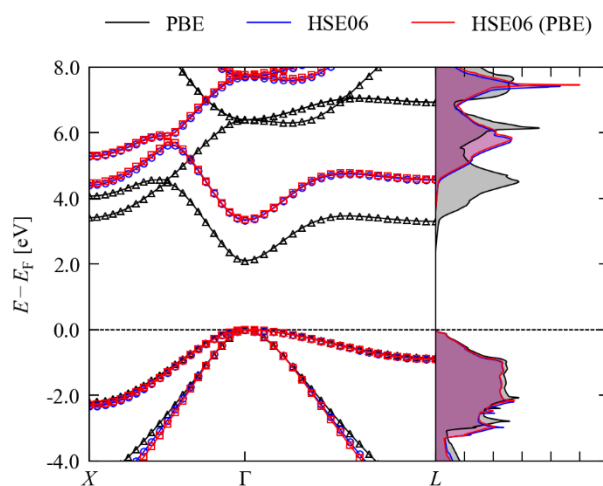


**Figure S4.13** Comparison of the electronic band dispersion and density of states  $g(E)$  for ZnS calculated using PBE (black), HSE06 (blue) and non-self-consistent HSE06 calculations using the PBE orbitals (red).

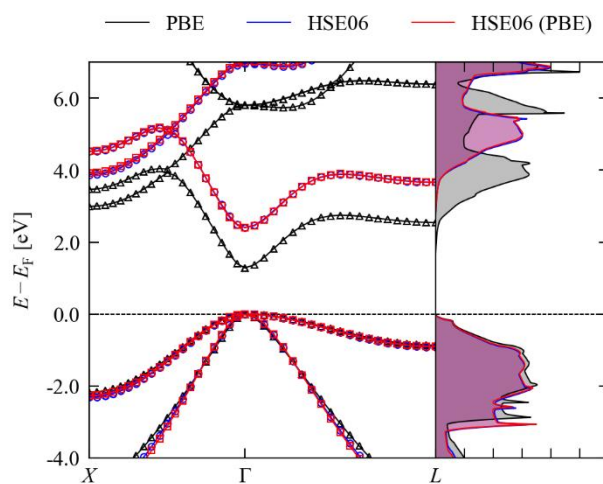


**Figure S4.14** Comparison of the electronic band dispersion and density of states  $g(E)$  for ZnSe calculated using PBE (black), HSE06 (blue) and non-self-consistent HSE06 calculations using the PBE orbitals (red).

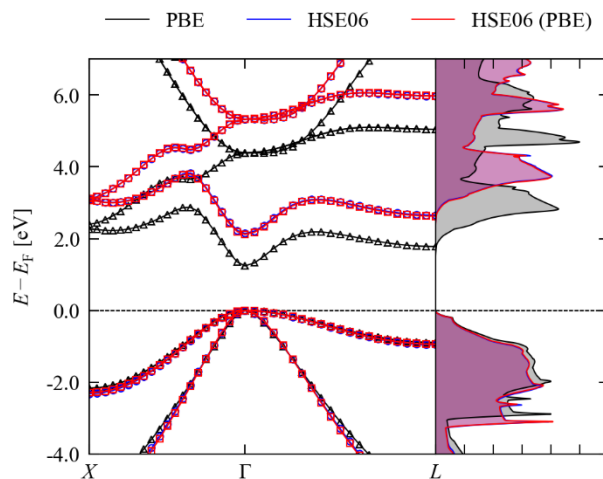


**Figure S4.15** Comparison of the electronic band dispersion and density of states  $g(E)$  for ZnTe calculated using PBE (black), HSE06 (blue) and non-self-consistent HSE06 calculations using the PBE orbitals (red).

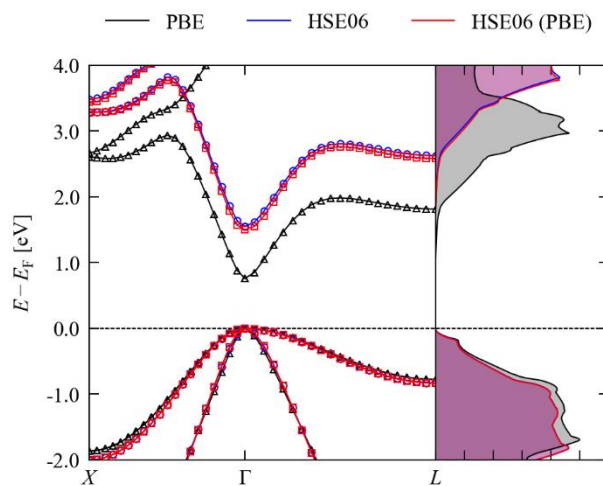


**Figure S4.16** Comparison of the electronic band dispersion and density of states  $g(E)$  for CdTe calculated using PBE (black), HSE06 (blue) and non-self-consistent HSE06 calculations using the PBE orbitals (red).

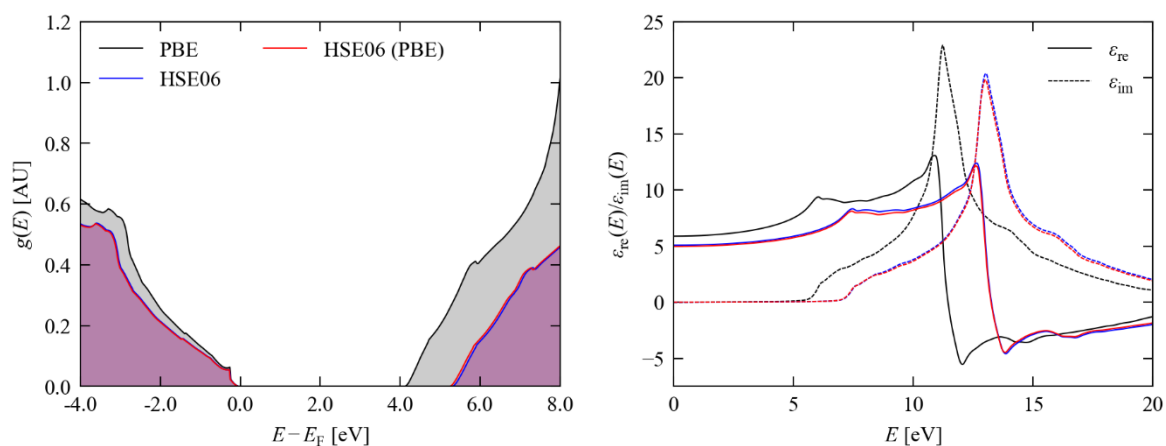


**Figure S4.17** Comparison of the density of states  $g(E)$  (a) and real and imaginary energy-dependent dielectric functions  $\epsilon_{re}(E)/\epsilon_{im}(E)$  (b) of C calculated using PBE (black), HSE06 (blue) and non-self-consistent HSE06 calculations using the PBE orbitals (red).

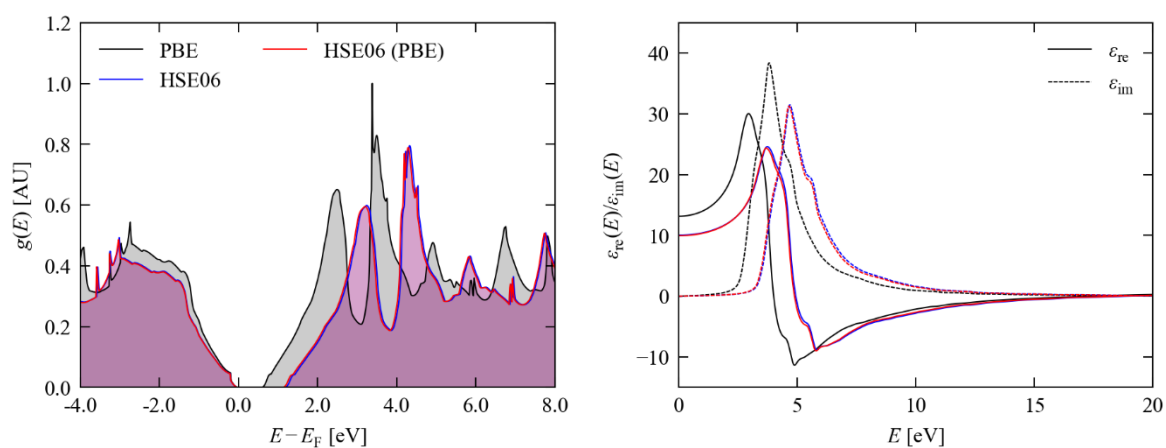


**Figure S4.18** Comparison of the density of states  $g(E)$  (a) and real and imaginary energy-dependent dielectric functions  $\epsilon_{re}(E)/\epsilon_{im}(E)$  (b) of Si calculated using PBE (black), HSE06 (blue) and non-self-consistent HSE06 calculations using the PBE orbitals (red).

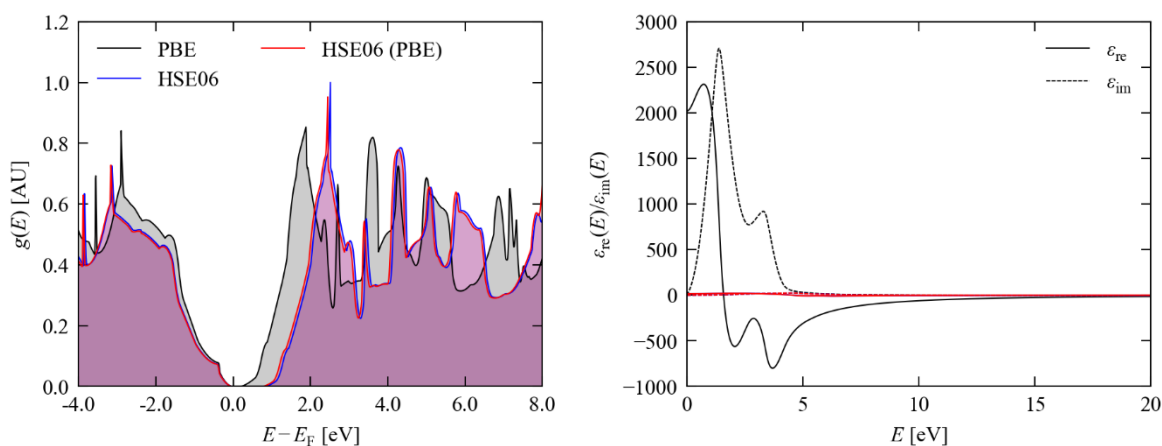


**Figure S4.19** Comparison of the density of states  $g(E)$  (a) and real and imaginary energy-dependent dielectric functions  $\epsilon_{re}(E)/\epsilon_{im}(E)$  (b) of Ge calculated using PBE (black), HSE06 (blue) and non-self-consistent HSE06 calculations using the PBE orbitals (red).

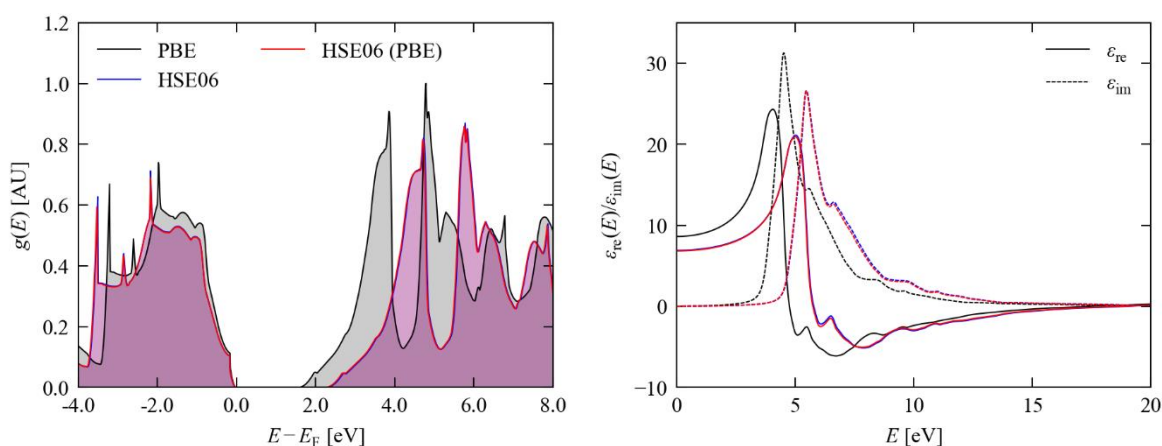


**Figure S4.20** Comparison of the density of states  $g(E)$  (a) and real and imaginary energy-dependent dielectric functions  $\epsilon_{re}(E)/\epsilon_{im}(E)$  (b) of AlP calculated using PBE (black), HSE06 (blue) and non-self-consistent HSE06 calculations using the PBE orbitals (red)

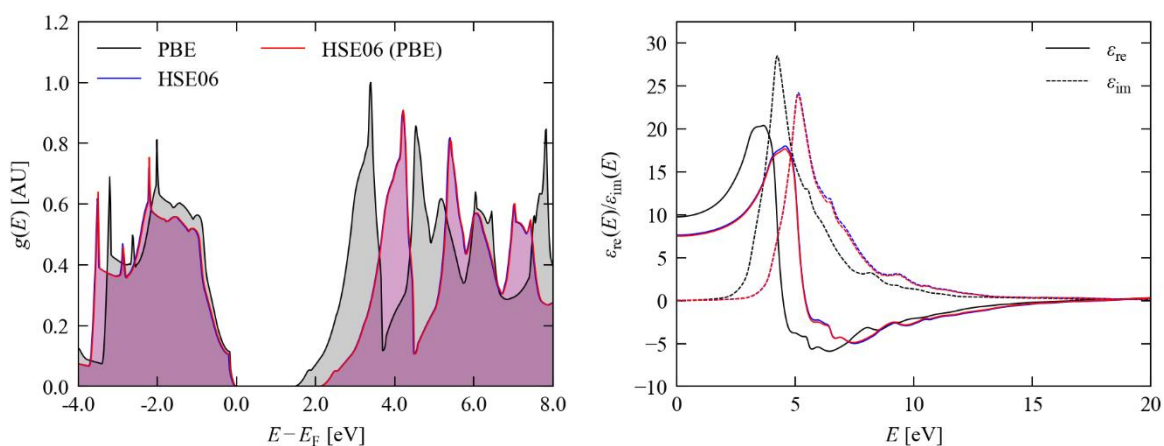


**Figure S4.21** Comparison of the density of states  $g(E)$  (a) and real and imaginary energy-dependent dielectric functions  $\epsilon_{re}(E)/\epsilon_{im}(E)$  (b) of AlAs calculated using PBE (black), HSE06 (blue) and non-self-consistent HSE06 calculations using the PBE orbitals (red).

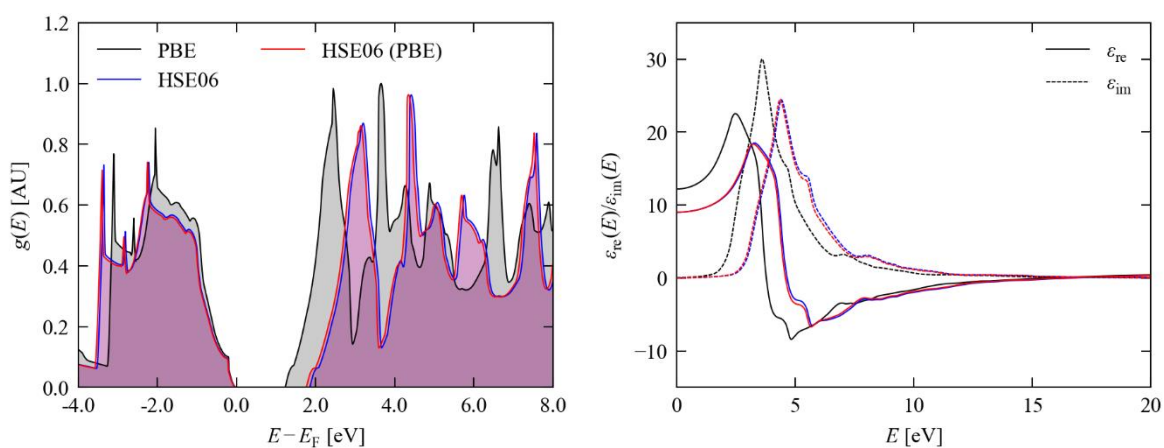


**Figure S4.22** Comparison of the density of states  $g(E)$  (a) and real and imaginary energy-dependent dielectric functions  $\epsilon_{re}(E)/\epsilon_{im}(E)$  (b) of AlSb calculated using PBE (black), HSE06 (blue) and non-self-consistent HSE06 calculations using the PBE orbitals (red).



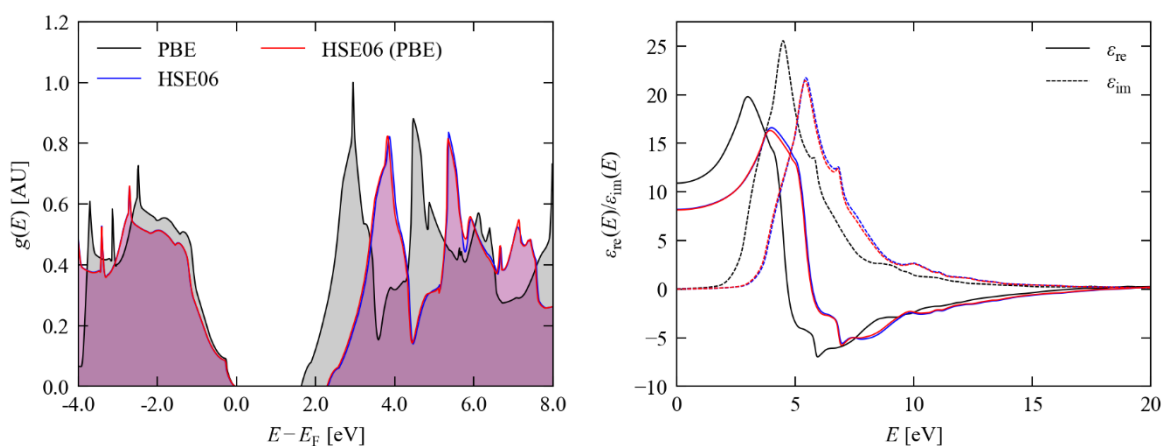


**Figure S4.23** Comparison of the density of states  $g(E)$  (a) and real and imaginary energy-dependent dielectric functions  $\epsilon_{\text{re}}(E)/\epsilon_{\text{im}}(E)$  (b) of GaP calculated using PBE (black), HSE06 (blue) and non-self-consistent HSE06 calculations using the PBE orbitals (red).

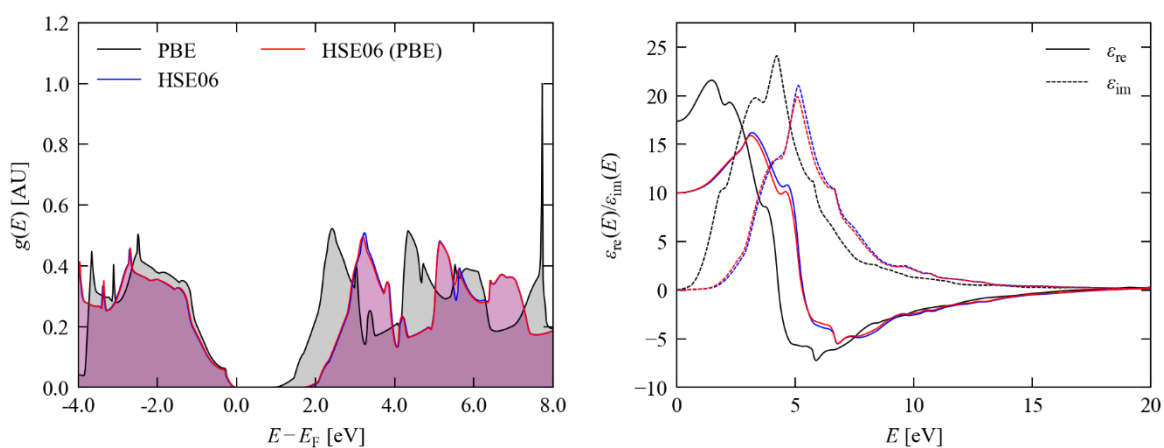


**Figure S4.24** Comparison of the density of states  $g(E)$  (a) and real and imaginary energy-dependent dielectric functions  $\epsilon_{\text{re}}(E)/\epsilon_{\text{im}}(E)$  (b) of GaAs calculated using PBE (black), HSE06 (blue) and non-self-consistent HSE06 calculations using the PBE orbitals (red).

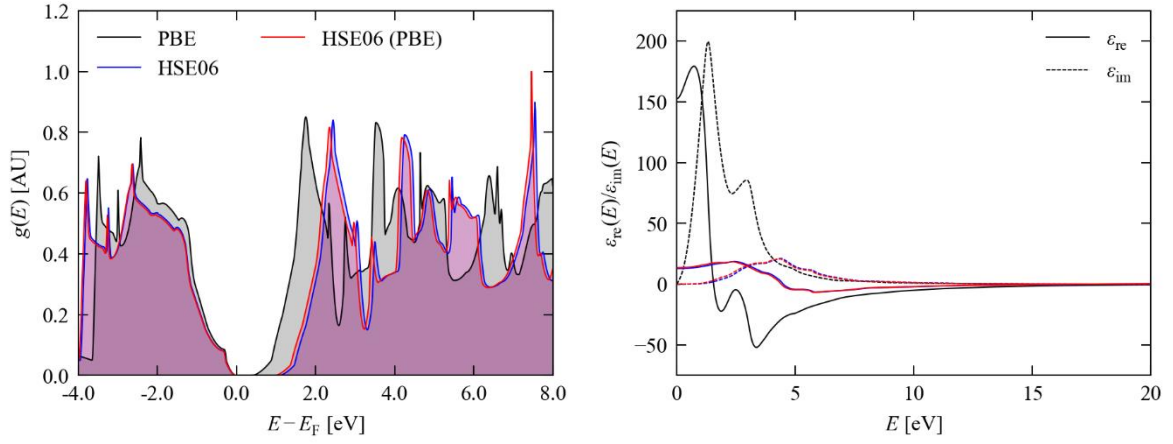


**Figure S4.25** Comparison of the density of states  $g(E)$  (a) and real and imaginary energy-dependent dielectric functions  $\epsilon_{re}(E)/\epsilon_{im}(E)$  (b) of GaSb calculated using PBE (black), HSE06 (blue) and non-self-consistent HSE06 calculations using the PBE orbitals (red).

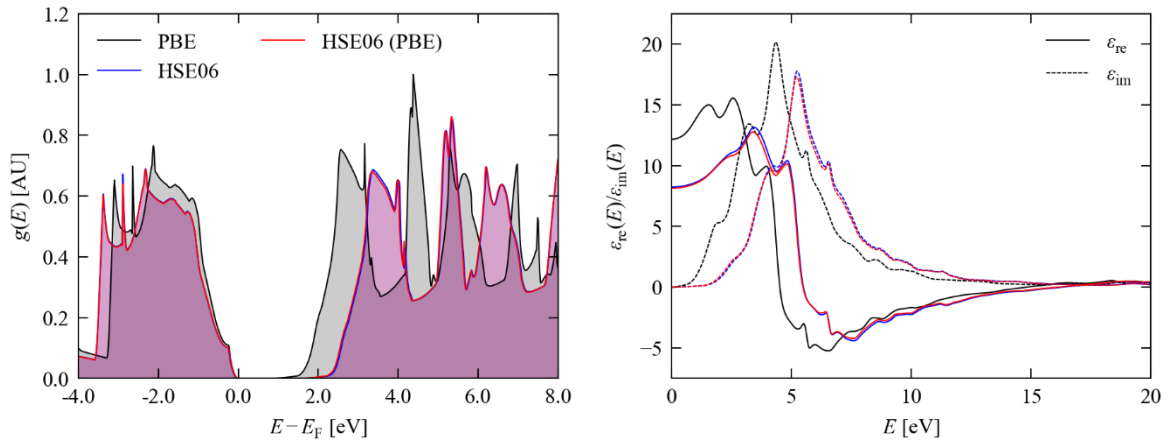


**Figure S4.26** Comparison of the density of states  $g(E)$  (a) and real and imaginary energy-dependent dielectric functions  $\epsilon_{re}(E)/\epsilon_{im}(E)$  (b) of InP calculated using PBE (black), HSE06 (blue) and non-self-consistent HSE06 calculations using the PBE orbitals (red).

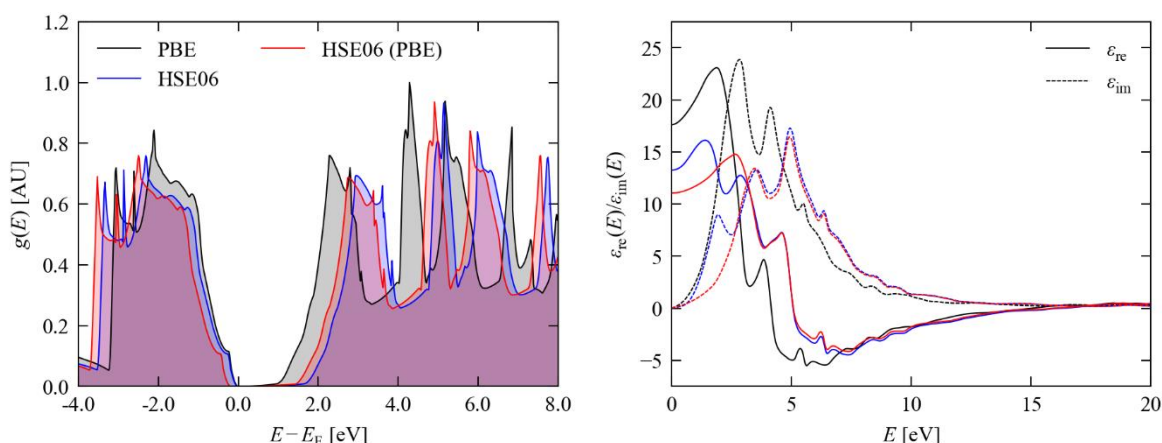


**Figure S4.27** Comparison of the density of states  $g(E)$  (a) and real and imaginary energy-dependent dielectric functions  $\epsilon_{\text{re}}(E)/\epsilon_{\text{im}}(E)$  (b) of InAs calculated using PBE (black), HSE06 (blue) and non-self-consistent HSE06 calculations using the PBE orbitals (red). The PBE functional predicts a metallic electronic structure for this compound, resulting in notably larger errors in the non-self-consistent calculations (see text).

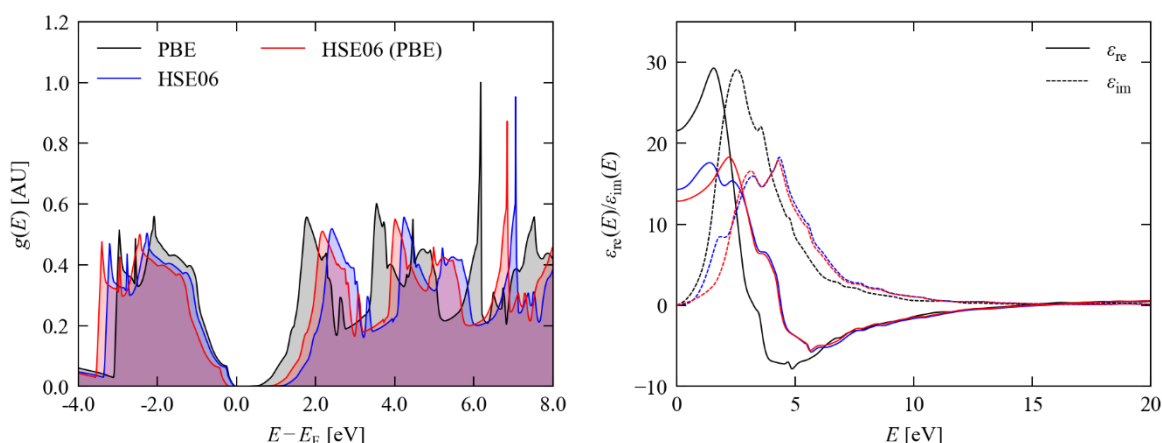


**Figure S4.28** Comparison of the density of states  $g(E)$  (a) and real and imaginary energy-dependent dielectric functions  $\epsilon_{\text{re}}(E)/\epsilon_{\text{im}}(E)$  (b) of InSb calculated using PBE (black), HSE06 (blue) and non-self-consistent HSE06 calculations using the PBE orbitals (red). The PBE functional predicts a metallic electronic structure for this compound, resulting in notably larger errors in the non-self-consistent calculations (see text).

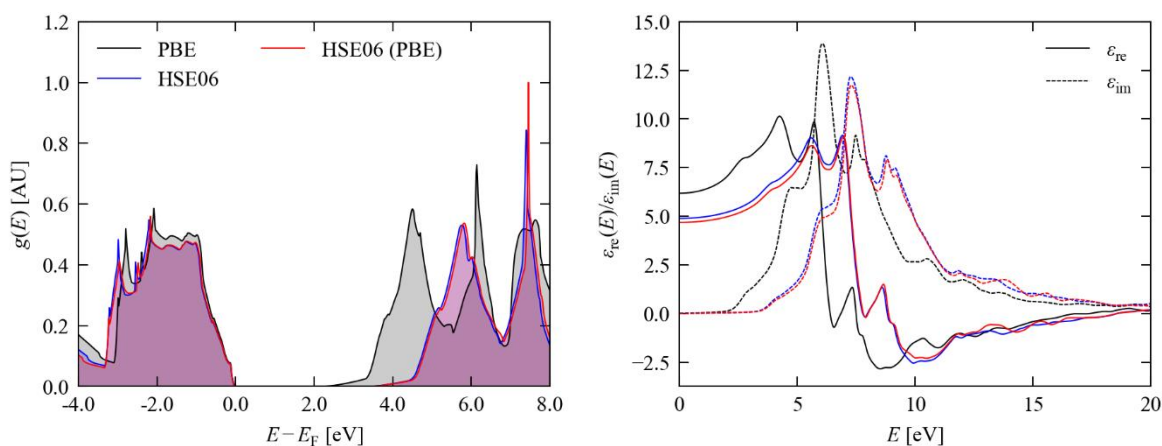


**Figure S4.29** Comparison of the density of states  $g(E)$  (a) and real and imaginary energy-dependent dielectric functions  $\epsilon_{re}(E)/\epsilon_{im}(E)$  (b) of ZnS calculated using PBE (black), HSE06 (blue) and non-self-consistent HSE06 calculations using the PBE orbitals (red).

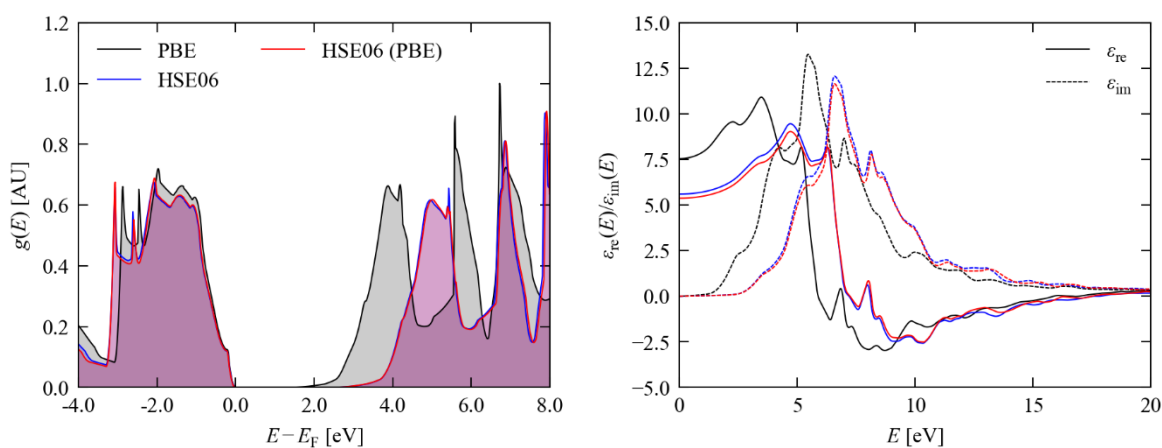


**Figure S4.30** Comparison of the density of states  $g(E)$  (a) and real and imaginary energy-dependent dielectric functions  $\epsilon_{re}(E)/\epsilon_{im}(E)$  (b) of ZnSe calculated using PBE (black), HSE06 (blue) and non-self-consistent HSE06 calculations using the PBE orbitals (red).

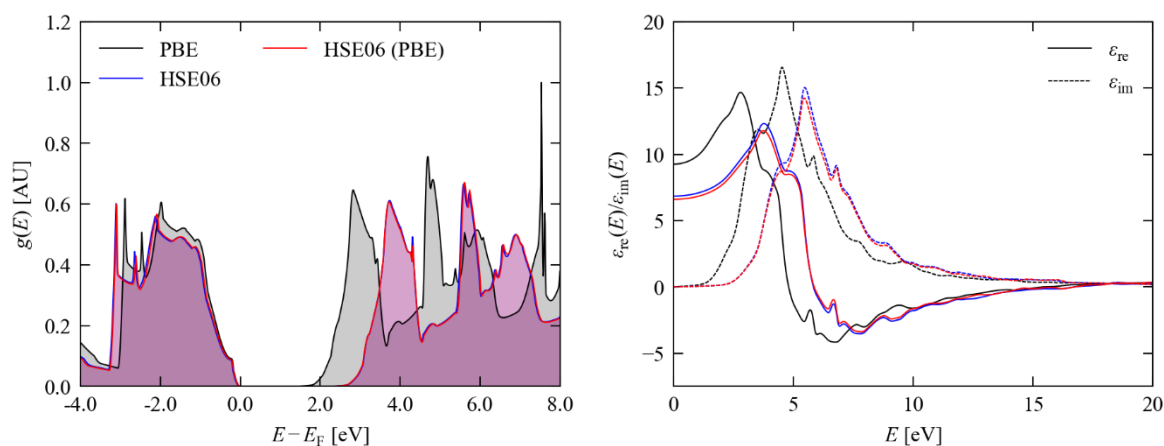


**Figure S4.31** Comparison of the density of states  $g(E)$  (a) and real and imaginary energy-dependent dielectric functions  $\epsilon_{re}(E)/\epsilon_{im}(E)$  (b) of ZnTe calculated using PBE (black), HSE06 (blue) and non-self-consistent HSE06 calculations using the PBE orbitals (red).

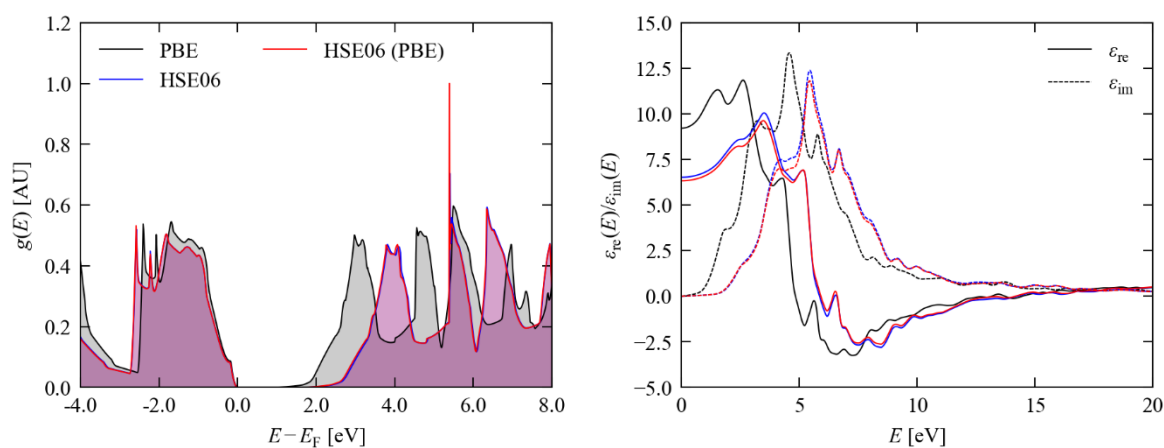


**Figure S4.32** Comparison of the density of states  $g(E)$  (a) and real and imaginary energy-dependent dielectric functions  $\epsilon_{re}(E)/\epsilon_{im}(E)$  (b) of CdTe calculated using PBE (black), HSE06 (blue) and non-self-consistent HSE06 calculations using the PBE orbitals (red).

## S5. Total Energies and Equations of State

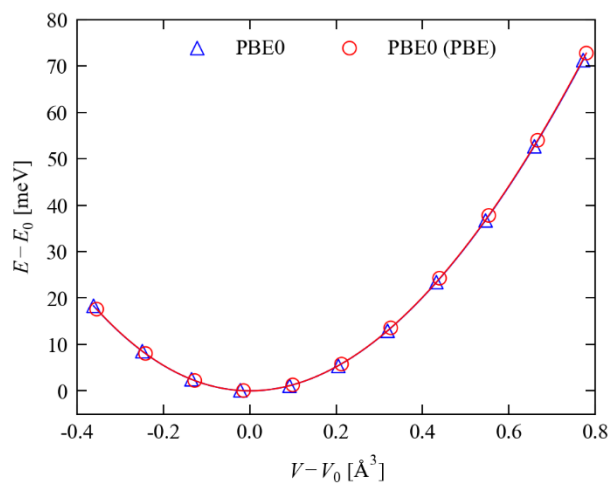


**Figure S5.1** Energy-volume curve for C obtained with PBE0<sup>8</sup> using self-consistent total energies (blue) and non-self-consistent energies calculated using the PBE<sup>1</sup> orbitals (red). The markers show the calculated energies and the solid lines are fits to the Birch-Murnaghan equation of state<sup>2</sup> (Eq. 6 in the text).

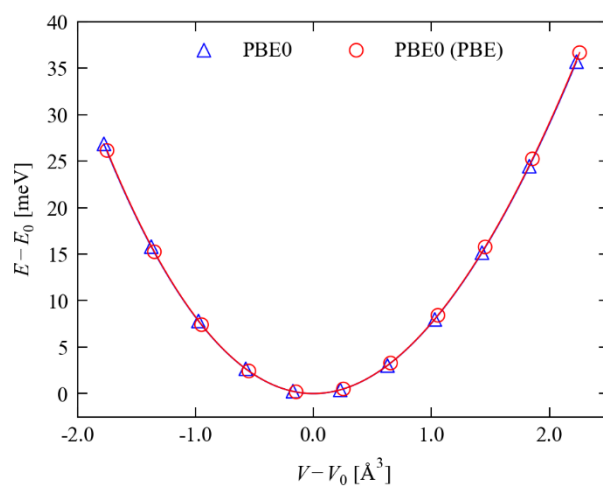


**Figure S5.2** Energy-volume curve for Si obtained with PBE0 using self-consistent total energies (blue) and non-self-consistent energies calculated using the PBE orbitals (red). The markers show the calculated energies and the solid lines are fits to the Birch-Murnaghan equation of state (Eq. 6 in the text).

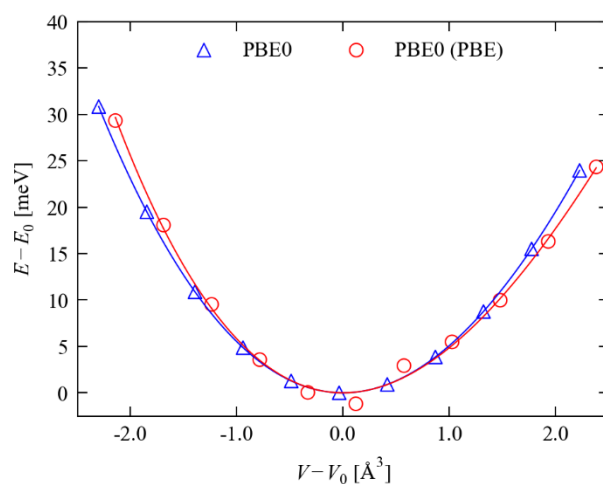


**Figure S5.3** Energy-volume curve for Ge obtained with PBE0 using self-consistent total energies (blue) and non-self-consistent energies calculated using the PBE orbitals (red). The markers show the calculated energies and the solid lines are fits to the Birch-Murnaghan equation of state (Eq. 6 in the text). PBE predicts a metallic electronic structure at some of the volume points, resulting in larger differences between the self-consistent and non-self-consistent results than in other compounds (see text).

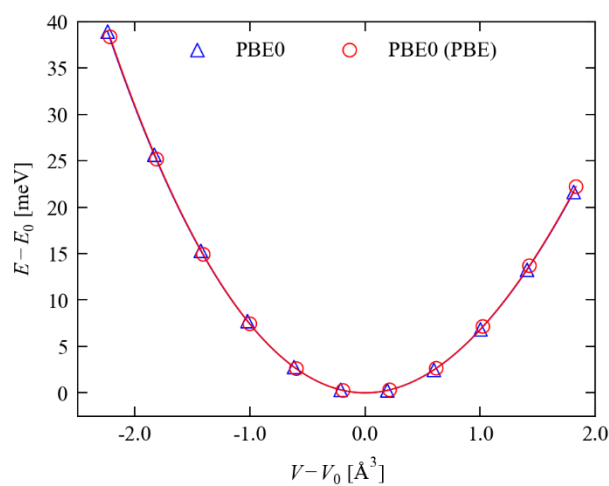


**Figure S5.4** Energy-volume curve for AlP obtained with PBE0 using self-consistent total energies (blue) and non-self-consistent energies calculated using the PBE orbitals (red). The markers show the calculated energies and the solid lines are fits to the Birch-Murnaghan equation of state (Eq. 6 in the text).

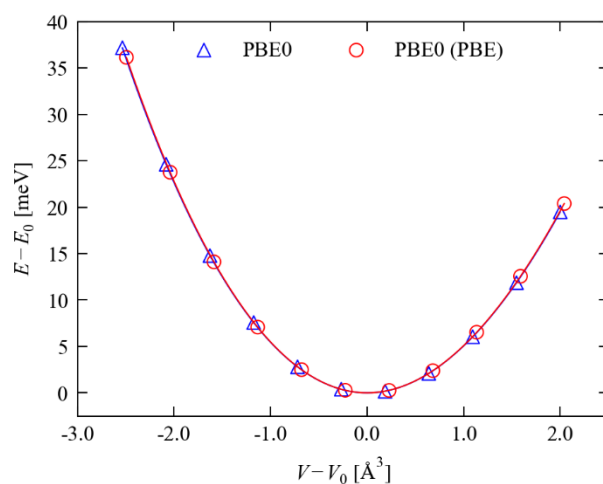


**Figure S5.5** Energy-volume curve for AlAs obtained with PBE0 using self-consistent total energies (blue) and non-self-consistent energies calculated using the PBE orbitals (red). The markers show the calculated energies and the solid lines are fits to the Birch-Murnaghan equation of state (Eq. 6 in the text).

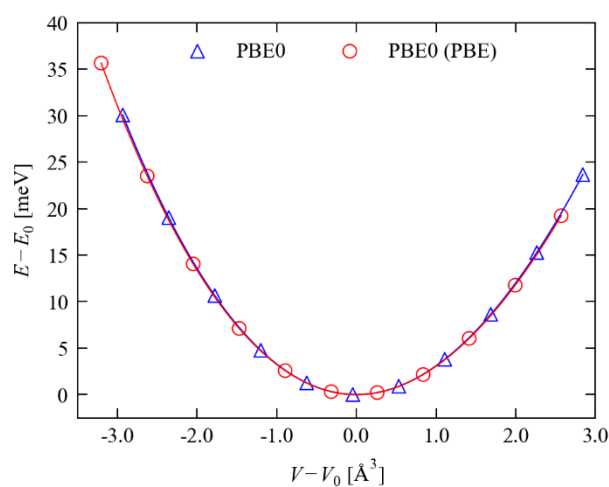


**Figure S5.6** Energy-volume curve for AlSb obtained with PBE0 using self-consistent total energies (blue) and non-self-consistent energies calculated using the PBE orbitals (red). The markers show the calculated energies and the solid lines are fits to the Birch-Murnaghan equation of state (Eq. 6 in the text).



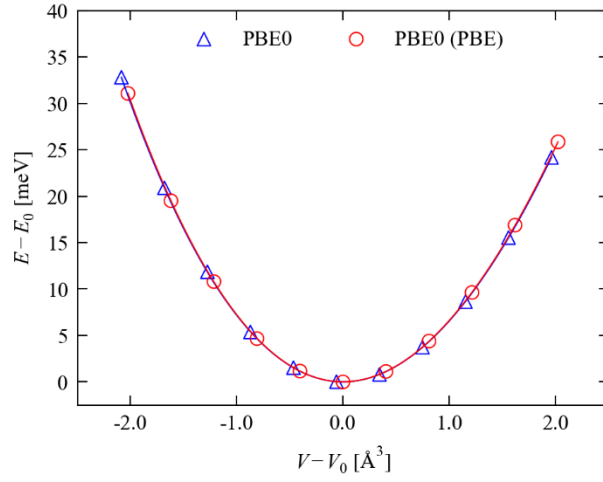


**Figure S5.7** Energy-volume curve for GaP obtained with PBE0 using self-consistent total energies (blue) and non-self-consistent energies calculated using the PBE orbitals (red). The markers show the calculated energies and the solid lines are fits to the Birch-Murnaghan equation of state (Eq. 6 in the text).

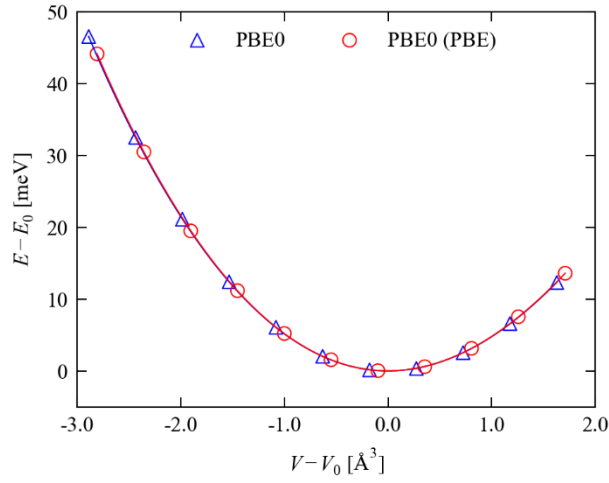


**Figure S5.8** Energy-volume curve for GaAs obtained with PBE0 using self-consistent total energies (blue) and non-self-consistent energies calculated using the PBE orbitals (red). The markers show the calculated energies and the solid lines are fits to the Birch-Murnaghan equation of state (Eq. 6 in the text).

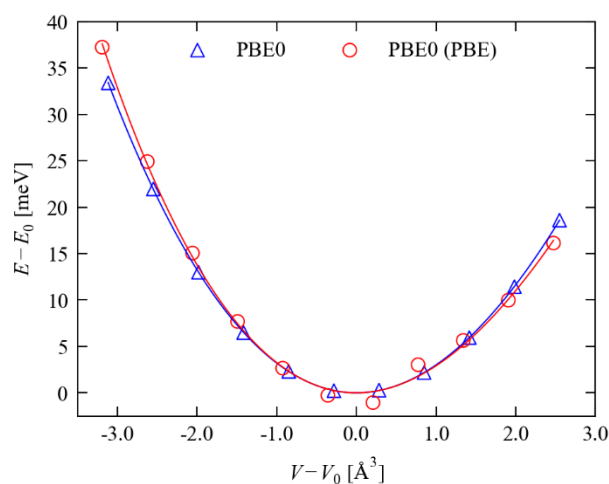


**Figure S5.9** Energy-volume curve for GaSb obtained with PBE0 using self-consistent total energies (blue) and non-self-consistent energies calculated using the PBE orbitals (red). The markers show the calculated energies and the solid lines are fits to the Birch-Murnaghan equation of state (Eq. 6 in the text). PBE predicts a metallic electronic structure at some of the volume points, resulting in larger differences between the self-consistent and non-self-consistent results than in other compounds (see text).

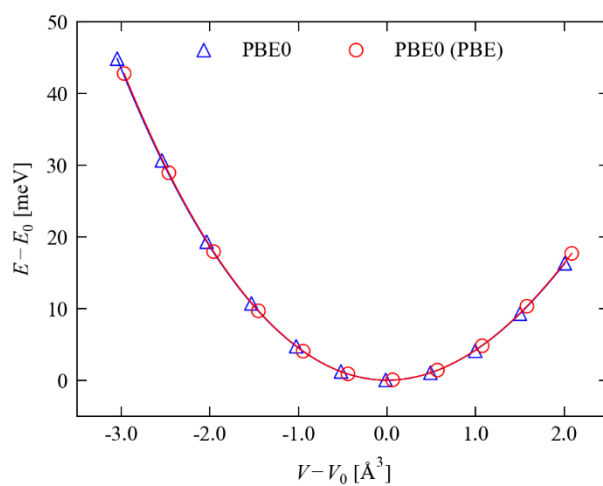


**Figure S5.10** Energy-volume curve for InP obtained with PBE0 using self-consistent total energies (blue) and non-self-consistent energies calculated using the PBE orbitals (red). The markers show the calculated energies and the solid lines are fits to the Birch-Murnaghan equation of state (Eq. 6 in the text).

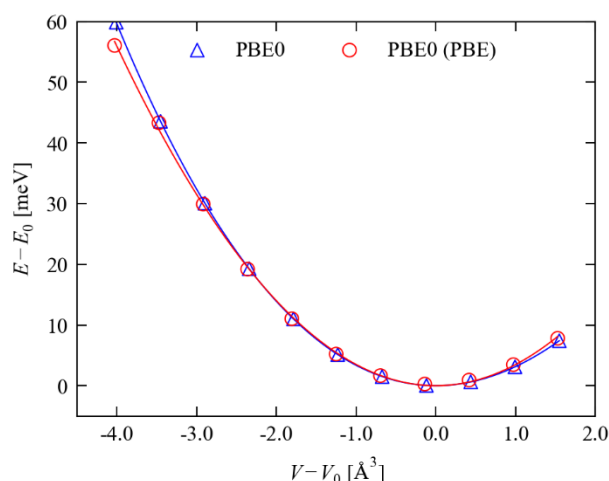


**Figure S5.11** Energy-volume curve for InAs obtained with PBE0 using self-consistent total energies (blue) and non-self-consistent energies calculated using the PBE orbitals (red). The markers show the calculated energies and the solid lines are fits to the Birch-Murnaghan equation of state (Eq. 6 in the text). PBE predicts a metallic electronic structure at some of the volume points, resulting in larger differences between the self-consistent and non-self-consistent results than in other compounds (see text).

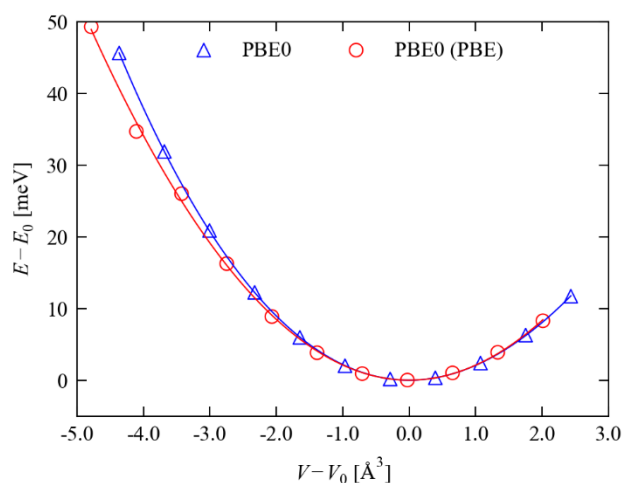


**Figure S5.12** Energy-volume curve for InSb obtained with PBE0 using self-consistent total energies (blue) and non-self-consistent energies calculated using the PBE orbitals (red). The markers show the calculated energies and the solid lines are fits to the Birch-Murnaghan equation of state (Eq. 6 in the text). PBE predicts a metallic electronic structure at some of the volume points, resulting in larger differences between the self-consistent and non-self-consistent results than in other compounds (see text).

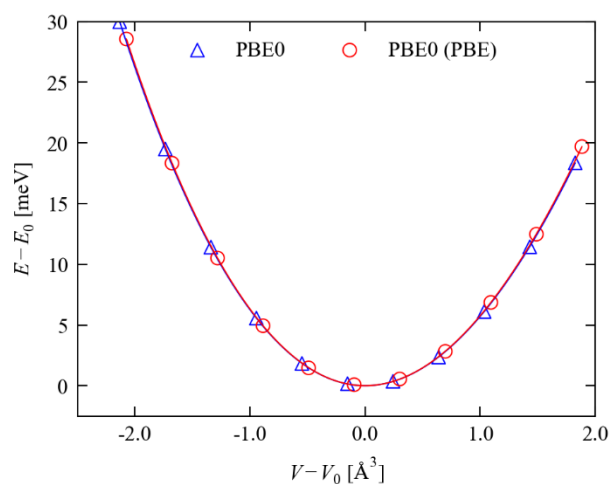


**Figure S5.13** Energy-volume curve for ZnS obtained with PBE0 using self-consistent total energies (blue) and non-self-consistent energies calculated using the PBE orbitals (red). The markers show the calculated energies and the solid lines are fits to the Birch-Murnaghan equation of state (Eq. 6 in the text).

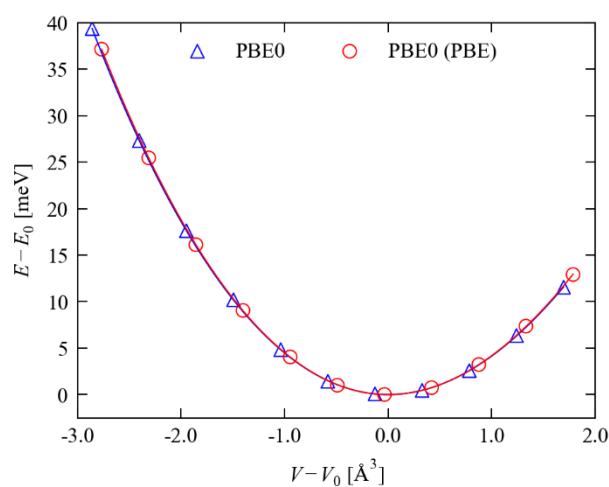


**Figure S5.14** Energy-volume curve for ZnSe obtained with PBE0 using self-consistent total energies (blue) and non-self-consistent energies calculated using the PBE orbitals (red). The markers show the calculated energies and the solid lines are fits to the Birch-Murnaghan equation of state (Eq. 6 in the text).

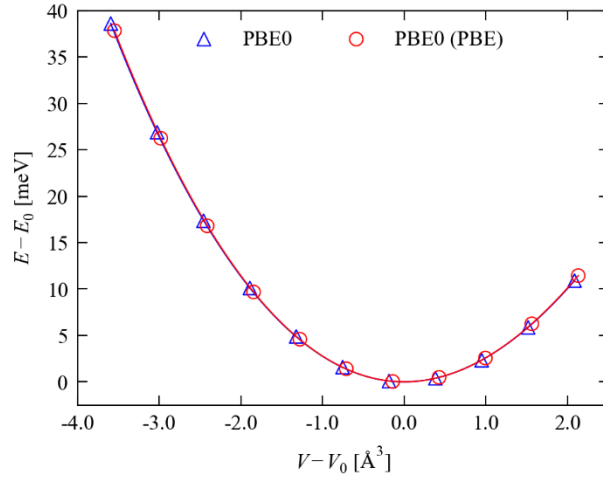


**Figure S5.15** Energy-volume curve for ZnTe obtained with PBE0 using self-consistent total energies (blue) and non-self-consistent energies calculated using the PBE orbitals (red). The markers show the calculated energies and the solid lines are fits to the Birch-Murnaghan equation of state (Eq. 6 in the text).

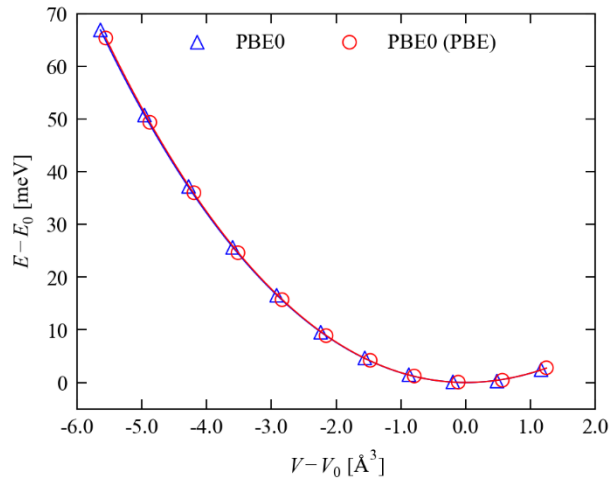


**Figure S5.16** Energy-volume curve for CdTe obtained with PBE0 using self-consistent total energies (blue) and non-self-consistent energies calculated using the PBE orbitals (red). The markers show the calculated energies and the solid lines are fits to the Birch-Murnaghan equation of state (Eq. 6 in the text).

## S6. Dielectric-Dependent Hybrid Functionals: scPBE0

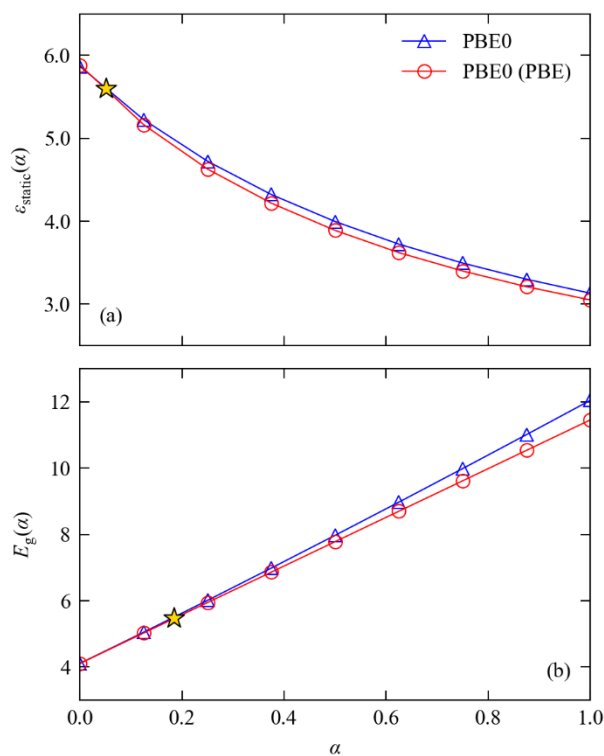


**Figure S6.1** Dependence of the calculated high-frequency dielectric constant  $\epsilon_{\infty}$  and bandgap  $E_g$  of C on the fraction of exact exchange  $\alpha$  used in the PBE0 hybrid functional (c.f. Eq. 7 in the text).<sup>8</sup> The self-consistent values and the non-self-consistent values obtained using the PBE<sup>1</sup> orbitals are shown as blue triangles and red circles, respectively, and the experimental values from Table 1 in the text are overlaid as gold stars.

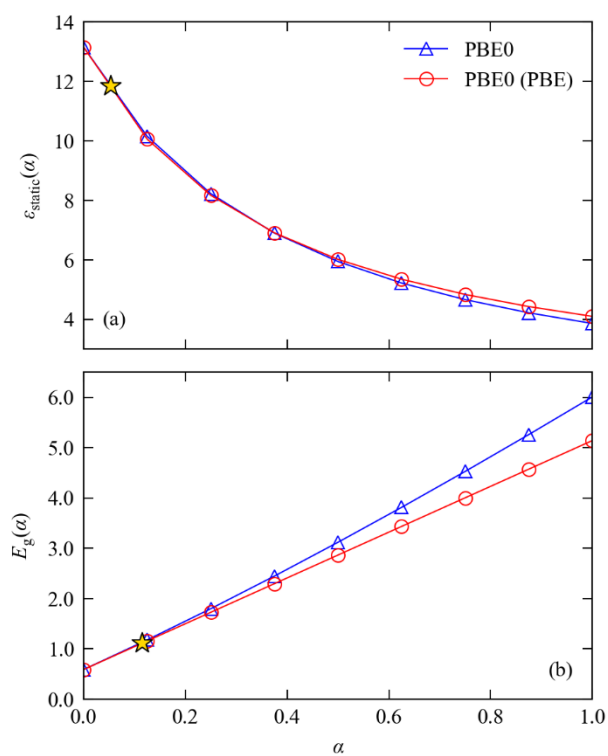


**Figure S6.2** Dependence of the calculated high-frequency dielectric constant  $\epsilon_{\infty}$  and bandgap  $E_g$  of Si on the fraction of exact exchange  $\alpha$  used in the PBE0 hybrid functional (c.f. Eq. 7 in the text). The self-consistent values and the non-self-consistent values obtained using the PBE orbitals are shown as blue triangles and red circles, respectively, and the experimental values from Table 1 in the text are overlaid as gold stars.

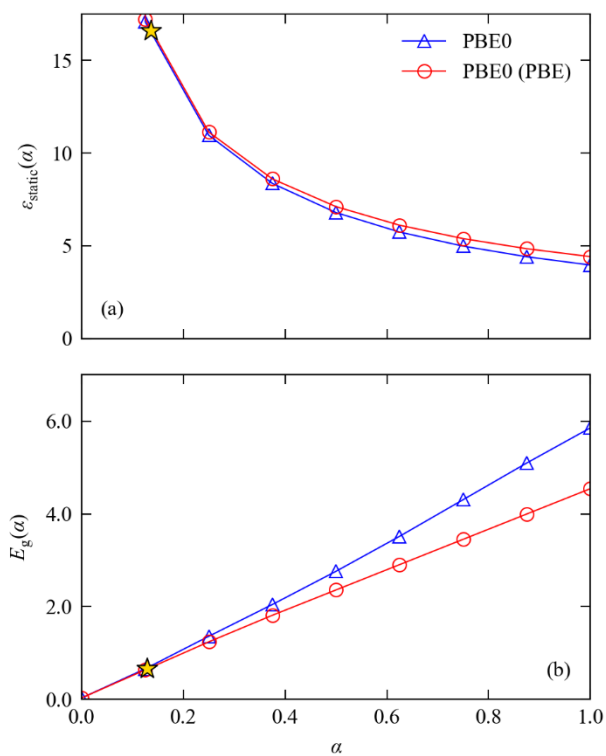


**Figure S6.3** Dependence of the calculated high-frequency dielectric constant  $\epsilon_{\infty}$  and bandgap  $E_g$  of Ge on the fraction of exact exchange  $\alpha$  used in the PBE0 hybrid functional (c.f. Eq. 7 in the text). The self-consistent values and the non-self-consistent values obtained using the PBE orbitals are shown as blue triangles and red circles, respectively, and the experimental values from Table 1 in the text are overlaid as gold stars.



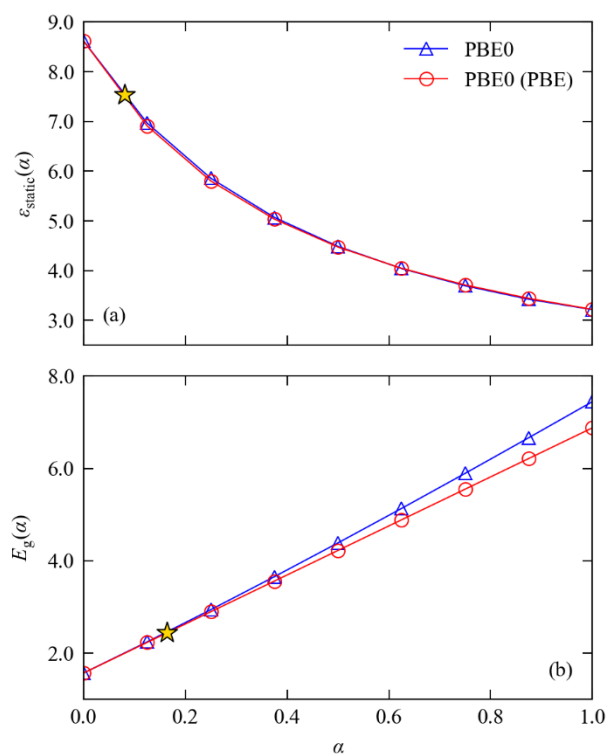


**Figure S6.4** Dependence of the calculated high-frequency dielectric constant  $\epsilon_{\infty}$  and bandgap  $E_g$  of AIP on the fraction of exact exchange  $\alpha$  used in the PBE0 hybrid functional (c.f. Eq. 7 in the text). The self-consistent values and the non-self-consistent values obtained using the PBE orbitals are shown as blue triangles and red circles, respectively, and the experimental values from Table 1 in the text are overlaid as gold stars.

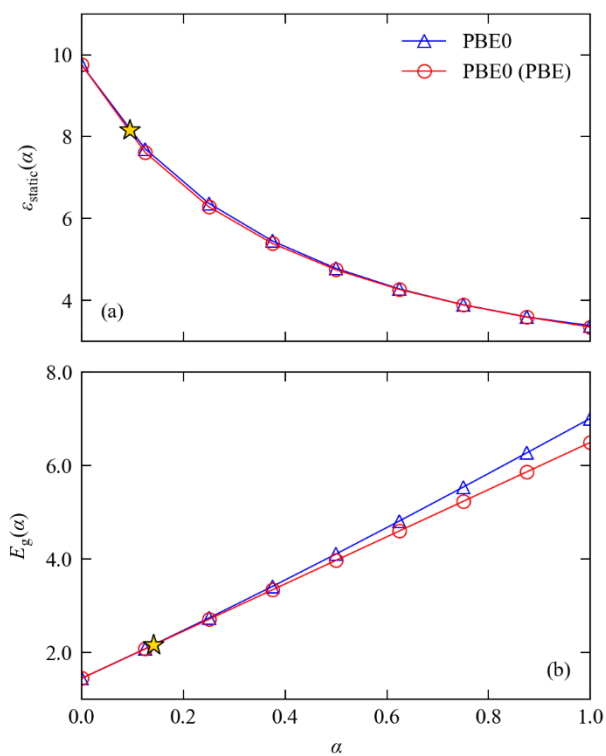


**Figure S6.5** Dependence of the calculated high-frequency dielectric constant  $\epsilon_{\infty}$  and bandgap  $E_g$  of AlAs on the fraction of exact exchange  $\alpha$  used in the PBE0 hybrid functional (c.f. Eq. 7 in the text). The self-consistent values and the non-self-consistent values obtained using the PBE orbitals are shown as blue triangles and red circles, respectively, and the experimental values from Table 1 in the text are overlaid as gold stars.

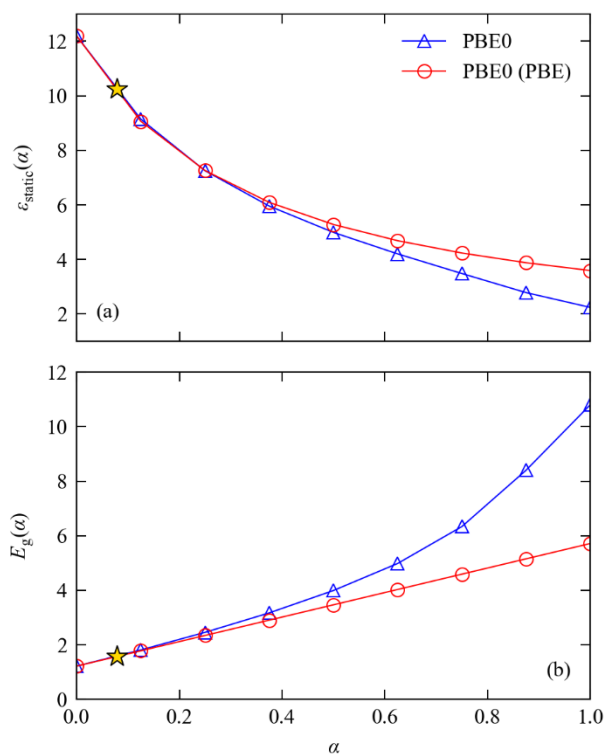


**Figure S6.6** Dependence of the calculated high-frequency dielectric constant  $\epsilon_{\infty}$  and bandgap  $E_g$  of AlSb on the fraction of exact exchange  $\alpha$  used in the PBE0 hybrid functional (c.f. Eq. 7 in the text). The self-consistent values and the non-self-consistent values obtained using the PBE orbitals are shown as blue triangles and red circles, respectively, and the experimental values from Table 1 in the text are overlaid as gold stars.

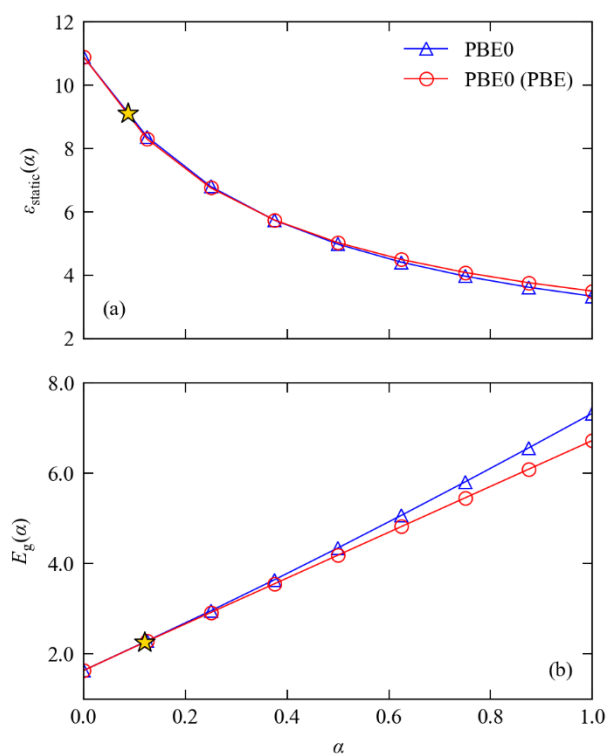


**Figure S6.7** Dependence of the calculated high-frequency dielectric constant  $\epsilon_{\infty}$  and bandgap  $E_g$  of GaP on the fraction of exact exchange  $\alpha$  used in the PBE0 hybrid functional (c.f. Eq. 7 in the text). The self-consistent values and the non-self-consistent values obtained using the PBE orbitals are shown as blue triangles and red circles, respectively, and the experimental values from Table 1 in the text are overlaid as gold stars.

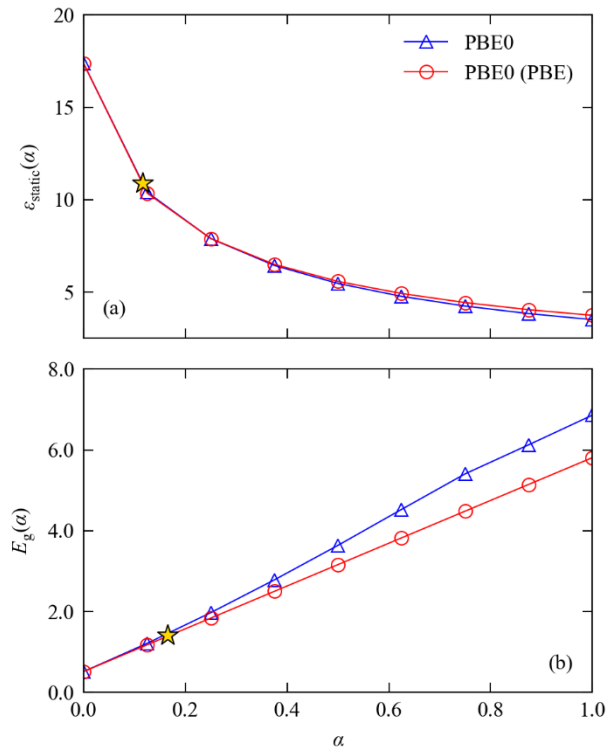


**Figure S6.8** Dependence of the calculated high-frequency dielectric constant  $\epsilon_{\infty}$  and bandgap  $E_g$  of GaAs on the fraction of exact exchange  $\alpha$  used in the PBE0 hybrid functional (c.f. Eq. 7 in the text). The self-consistent values and the non-self-consistent values obtained using the PBE orbitals are shown as blue triangles and red circles, respectively, and the experimental values from Table 1 in the text are overlaid as gold stars.

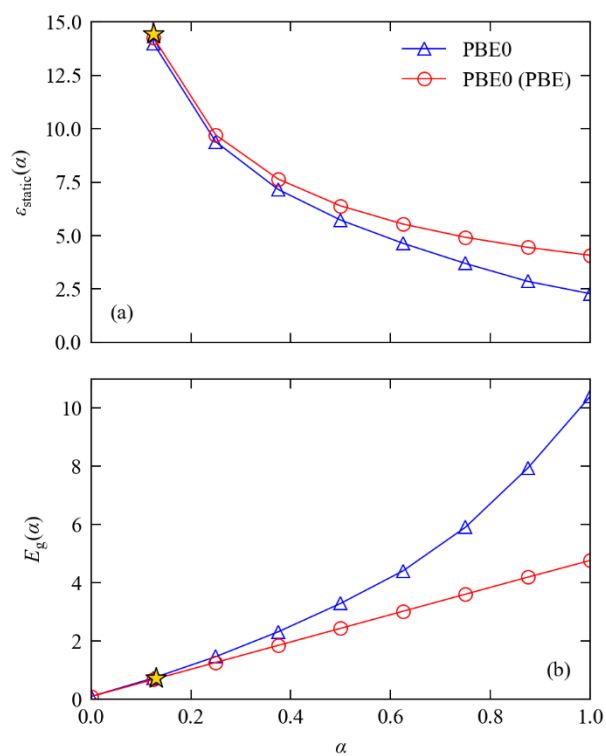


**Figure S6.9** Dependence of the calculated high-frequency dielectric constant  $\epsilon_{\infty}$  and bandgap  $E_g$  of GaSb on the fraction of exact exchange  $\alpha$  used in the PBE0 hybrid functional (c.f. Eq. 7 in the text). The self-consistent values and the non-self-consistent values obtained using the PBE orbitals are shown as blue triangles and red circles, respectively, and the experimental values from Table 1 in the text are overlaid as gold stars.

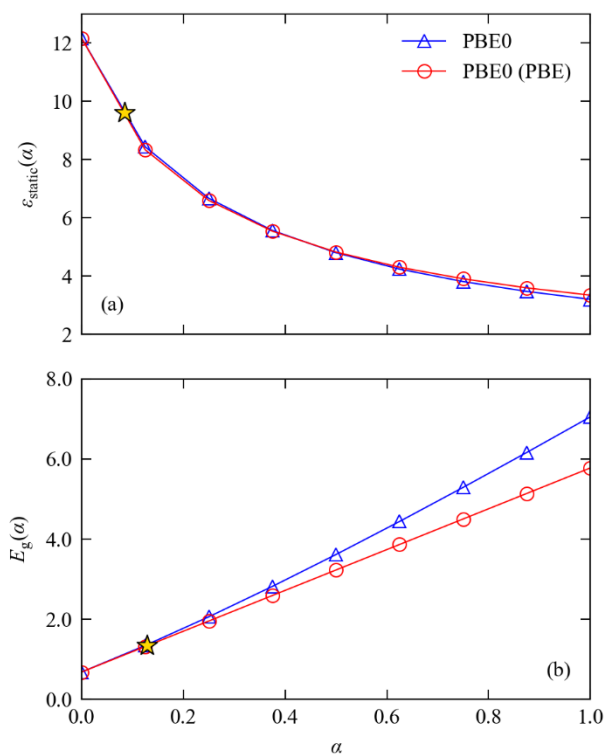


**Figure S6.10** Dependence of the calculated high-frequency dielectric constant  $\epsilon_{\infty}$  and bandgap  $E_g$  of InP on the fraction of exact exchange  $\alpha$  used in the PBE0 hybrid functional (c.f. Eq. 7 in the text). The self-consistent values and the non-self-consistent values obtained using the PBE orbitals are shown as blue triangles and red circles, respectively, and the experimental values from Table 1 in the text are overlaid as gold stars.

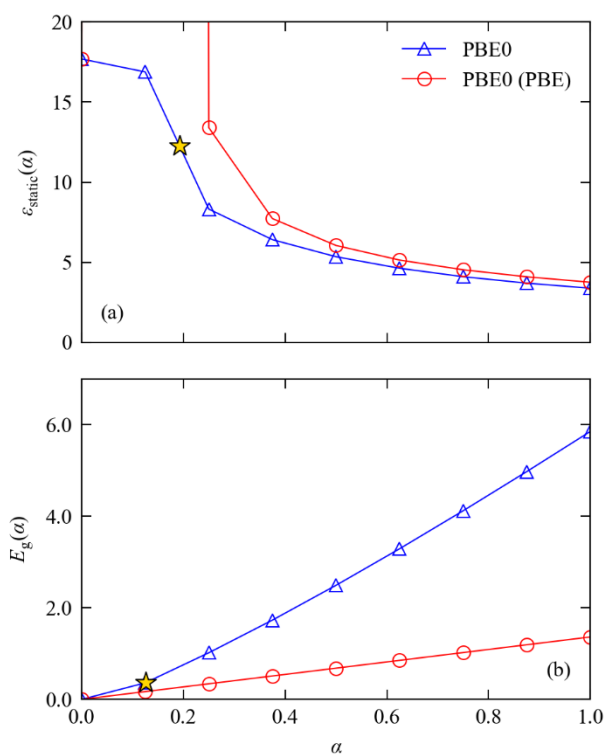


**Figure S6.11** Dependence of the calculated high-frequency dielectric constant  $\epsilon_{\infty}$  and bandgap  $E_g$  of InAs on the fraction of exact exchange  $\alpha$  used in the PBE0 hybrid functional (c.f. Eq. 7 in the text). The self-consistent values and the non-self-consistent values obtained using the PBE orbitals are shown as blue triangles and red circles, respectively, and the experimental values from Table 1 in the text are overlaid as gold stars. Note that PBE predicts a metallic electronic structure for this system, resulting in anomalously large errors in the non-self-consistent calculations (see text).



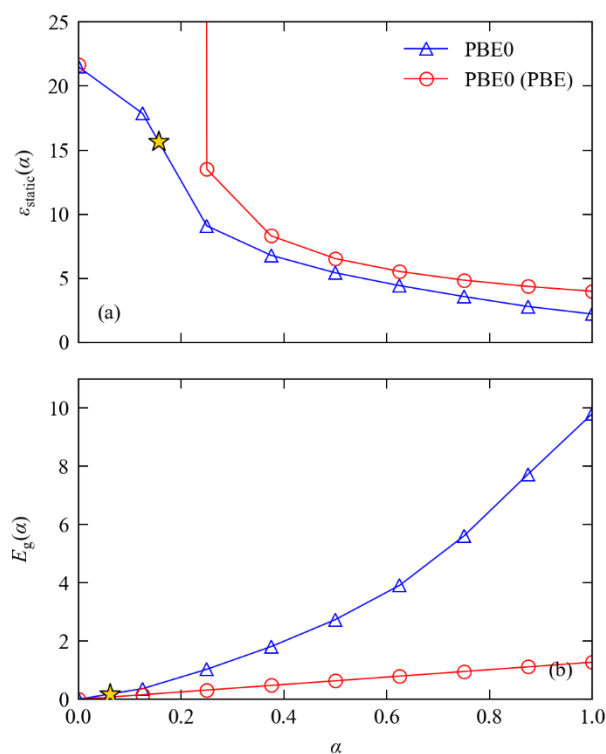


**Figure S6.12** Dependence of the calculated high-frequency dielectric constant  $\epsilon_{\infty}$  and bandgap  $E_g$  of InSb on the fraction of exact exchange  $\alpha$  used in the PBE0 hybrid functional (c.f. Eq. 7 in the text). The self-consistent values and the non-self-consistent values obtained using the PBE orbitals are shown as blue triangles and red circles, respectively, and the experimental values from Table 1 in the text are overlaid as gold stars. Note that PBE predicts a metallic electronic structure for this system, resulting in anomalously large errors in the non-self-consistent calculations (see text).

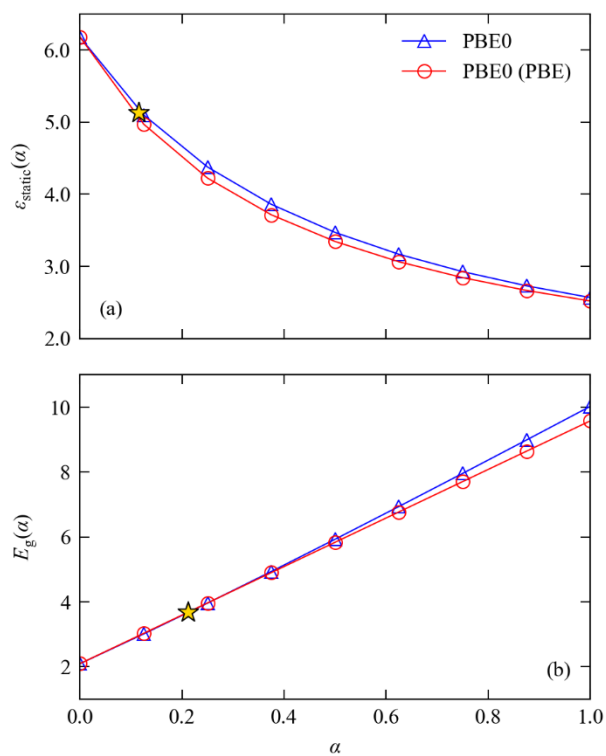


**Figure S6.13** Dependence of the calculated high-frequency dielectric constant  $\epsilon_{\infty}$  and bandgap  $E_g$  of ZnS on the fraction of exact exchange  $\alpha$  used in the PBE0 hybrid functional (c.f. Eq. 7 in the text). The self-consistent values and the non-self-consistent values obtained using the PBE orbitals are shown as blue triangles and red circles, respectively, and the experimental values from Table 1 in the text are overlaid as gold stars.

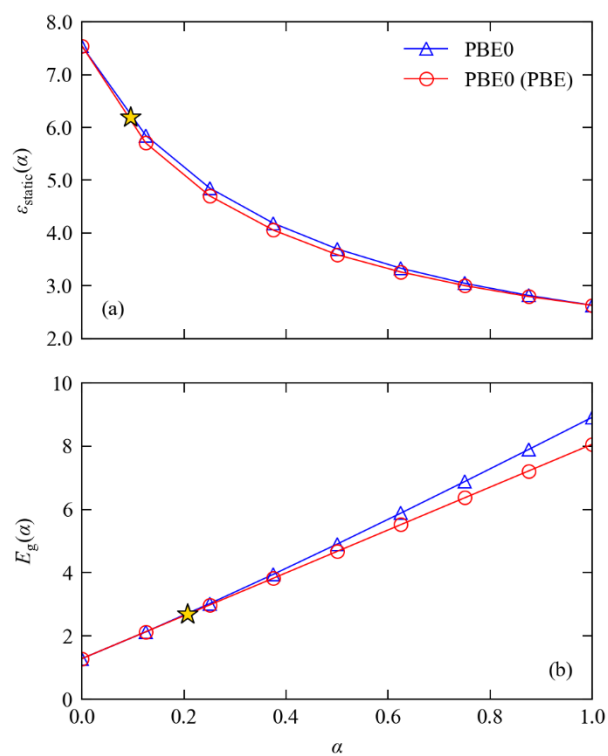


**Figure S6.14** Dependence of the calculated high-frequency dielectric constant  $\epsilon_{\infty}$  and bandgap  $E_g$  of ZnSe on the fraction of exact exchange  $\alpha$  used in the PBE0 hybrid functional (c.f. Eq. 7 in the text). The self-consistent values and the non-self-consistent values obtained using the PBE orbitals are shown as blue triangles and red circles, respectively, and the experimental values from Table 1 in the text are overlaid as gold stars.

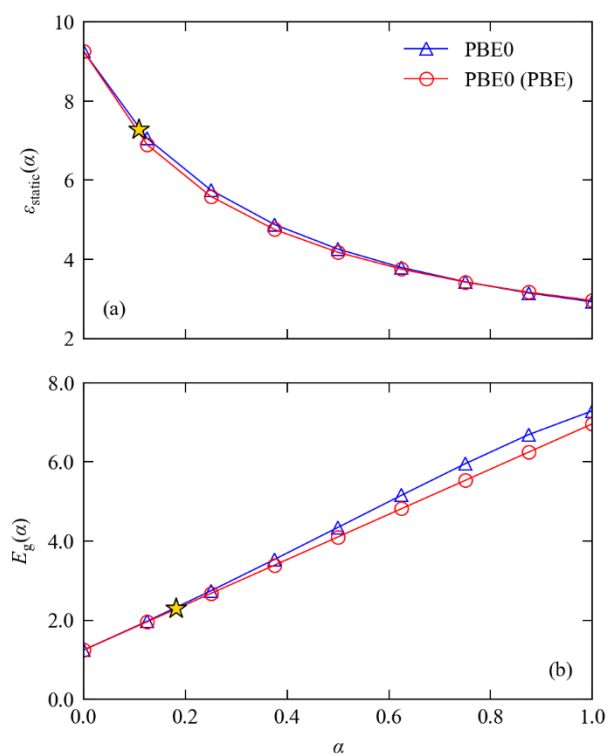


**Figure S6.15** Dependence of the calculated high-frequency dielectric constant  $\epsilon_{\infty}$  and bandgap  $E_g$  of ZnTe on the fraction of exact exchange  $\alpha$  used in the PBE0 hybrid functional (c.f. Eq. 7 in the text). The self-consistent values and the non-self-consistent values obtained using the PBE orbitals are shown as blue triangles and red circles, respectively, and the experimental values from Table 1 in the text are overlaid as gold stars.

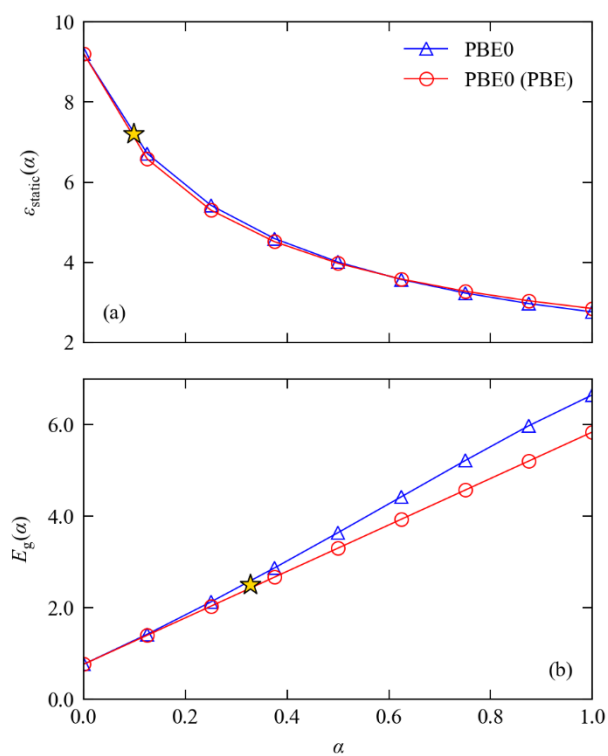


**Figure S6.16** Dependence of the calculated high-frequency dielectric constant  $\epsilon_{\infty}$  and bandgap  $E_g$  of CdTe on the fraction of exact exchange  $\alpha$  used in the PBE0 hybrid functional (c.f. Eq. 7 in the text). The self-consistent values and the non-self-consistent values obtained using the PBE orbitals are shown as blue triangles and red circles, respectively, and the experimental values from Table 1 in the text are overlaid as gold stars.

## S7. Partial Self-Consistency

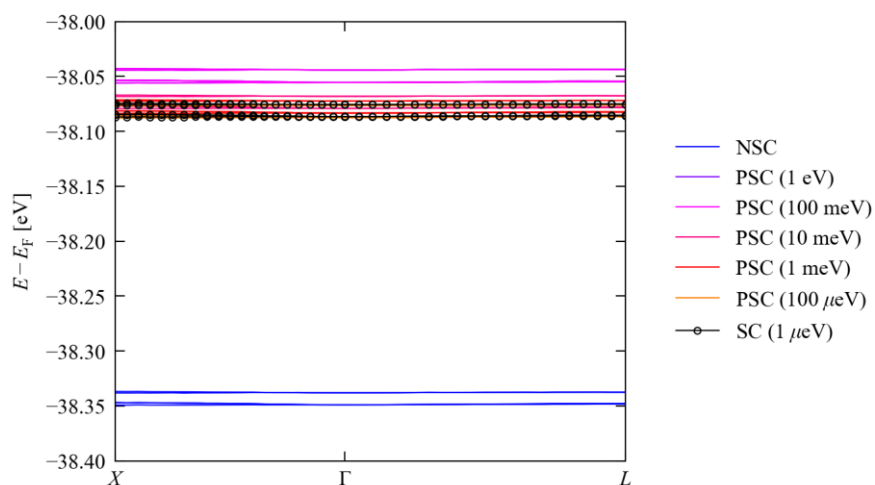


**Figure S7.1** Change in the dispersion of the semi-core As d bands in AlAs calculated using non-self-consistent and partially-self-consistent HSE06 starting from the PBE orbitals with SCF convergence thresholds of 1 eV to 100  $\mu\text{eV}$  ( $10^0 - 10^{-4}$  eV). The black lines with markers show the reference dispersion obtained from fully self-consistent calculations performed to a tolerance of 1  $\mu\text{eV}$  ( $10^{-6}$  eV).

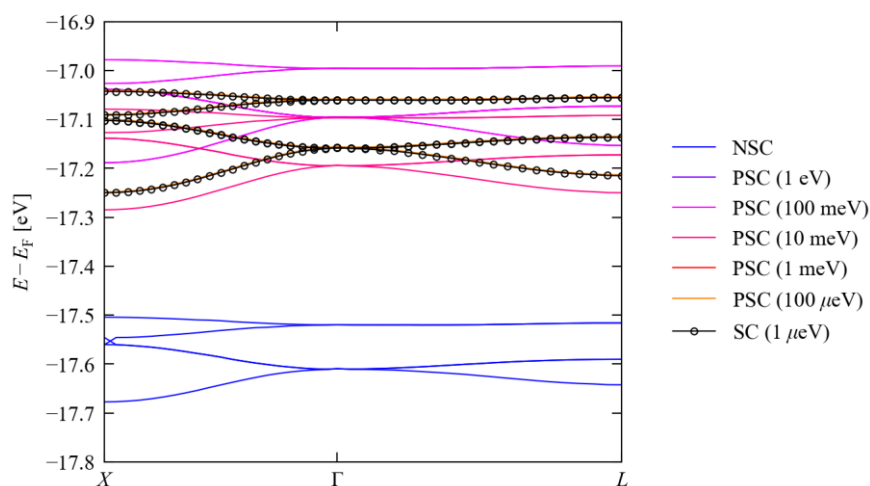


**Figure S7.2** Change in the dispersion of the semi-core Ga d bands in GaP calculated using non-self-consistent and partially-self-consistent HSE06 starting from the PBE orbitals with SCF convergence thresholds of 1 eV to 100  $\mu\text{eV}$  ( $10^0 - 10^{-4}$  eV). The black lines with markers show the reference dispersion obtained from fully self-consistent calculations performed to a tolerance of 1  $\mu\text{eV}$  ( $10^{-6}$  eV).

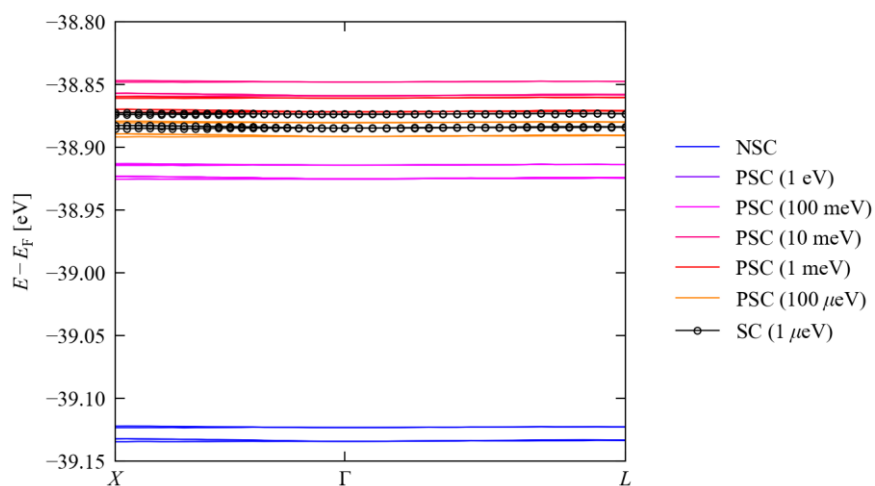


**Figure S7.3** Change in the dispersion of the semi-core As d bands in GaAs calculated using non-self-consistent and partially-self-consistent HSE06 starting from the PBE orbitals with SCF convergence thresholds of 1 eV to 100  $\mu\text{eV}$  ( $10^0 - 10^{-4}$  eV). The black lines with markers show the reference dispersion obtained from fully self-consistent calculations performed to a tolerance of 1  $\mu\text{eV}$  ( $10^{-6}$  eV).

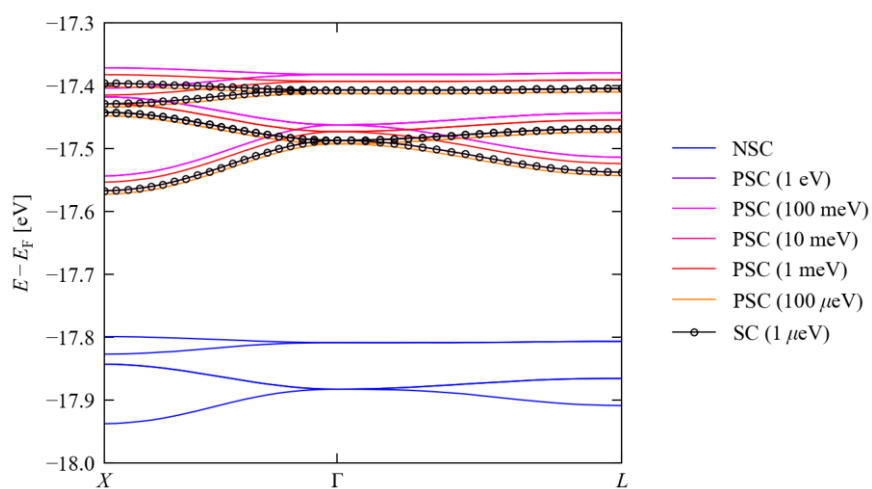


**Figure S7.4** Change in the dispersion of the semi-core Ga d bands in GaAs calculated using non-self-consistent and partially-self-consistent HSE06 starting from the PBE orbitals with SCF convergence thresholds of 1 eV to 100  $\mu\text{eV}$  ( $10^0 - 10^{-4}$  eV). The black lines with markers show the reference dispersion obtained from fully self-consistent calculations performed to a tolerance of 1  $\mu\text{eV}$  ( $10^{-6}$  eV).

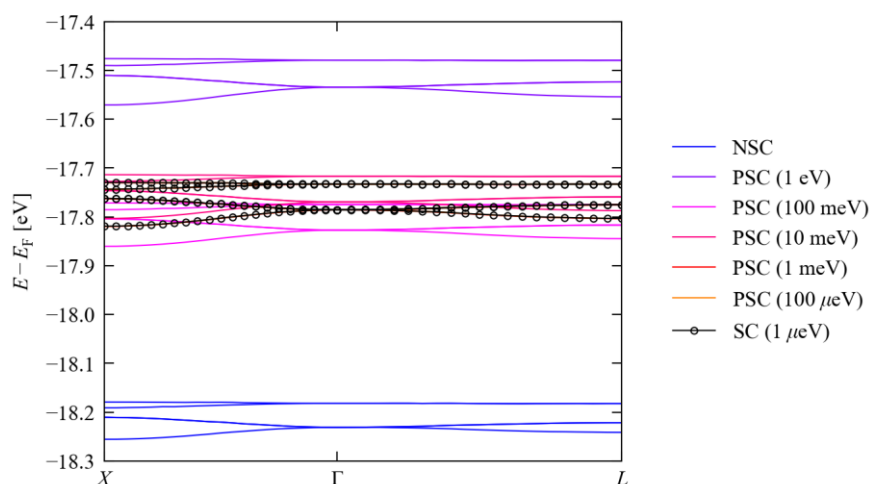


**Figure S7.5** Change in the dispersion of the semi-core Ga d bands in GaSb calculated using non-self-consistent and partially-self-consistent HSE06 starting from the PBE orbitals with SCF convergence thresholds of 1 eV to 100  $\mu\text{eV}$  ( $10^0 - 10^{-4}$  eV). The black lines with markers show the reference dispersion obtained from fully self-consistent calculations performed to a tolerance of 1  $\mu\text{eV}$  ( $10^{-6}$  eV).

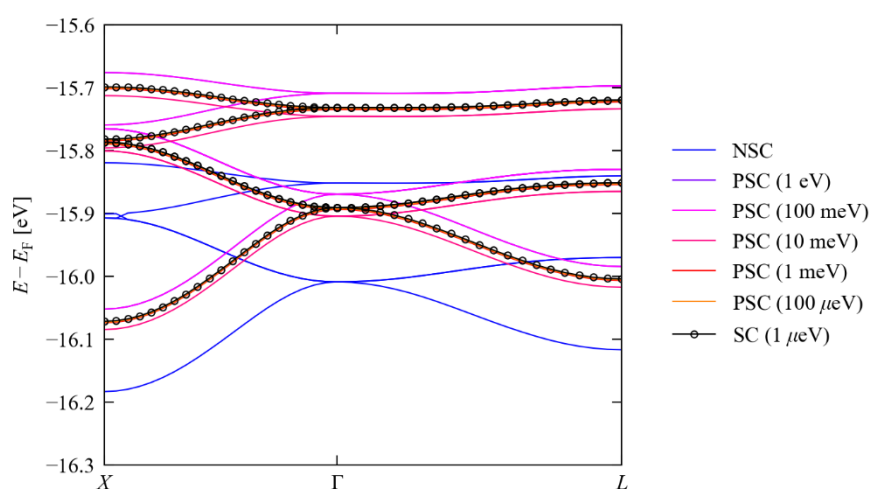


**Figure S7.6** Change in the dispersion of the semi-core In d bands in InP calculated using non-self-consistent and partially-self-consistent HSE06 starting from the PBE orbitals with SCF convergence thresholds of 1 eV to 100  $\mu\text{eV}$  ( $10^0 - 10^{-4}$  eV). The black lines with markers show the reference dispersion obtained from fully self-consistent calculations performed to a tolerance of 1  $\mu\text{eV}$  ( $10^{-6}$  eV).



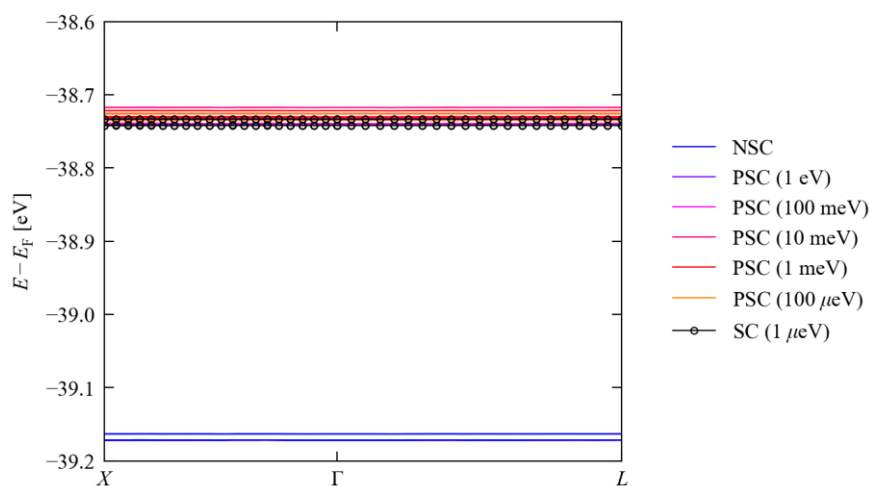


**Figure S7.7** Change in the dispersion of the semi-core As d bands in InAs calculated using non-self-consistent and partially-self-consistent HSE06 starting from the PBE orbitals with SCF convergence thresholds of 1 eV to 100  $\mu\text{eV}$  ( $10^0 - 10^{-4}$  eV). The black lines with markers show the reference dispersion obtained from fully self-consistent calculations performed to a tolerance of 1  $\mu\text{eV}$  ( $10^{-6}$  eV).

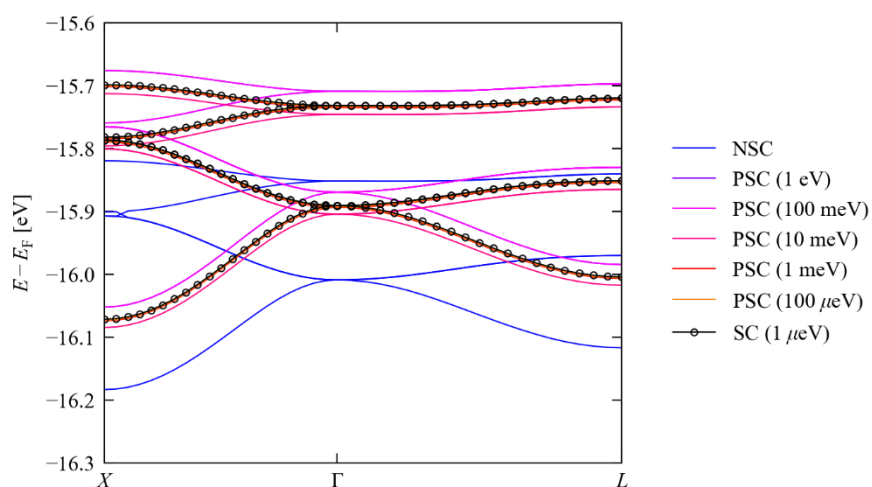


**Figure S7.8** Change in the dispersion of the semi-core In d bands in InAs calculated using non-self-consistent and partially-self-consistent HSE06 starting from the PBE orbitals with SCF convergence thresholds of 1 eV to 100  $\mu\text{eV}$  ( $10^0 - 10^{-4}$  eV). The black lines with markers show the reference dispersion obtained from fully self-consistent calculations performed to a tolerance of 1  $\mu\text{eV}$  ( $10^{-6}$  eV).

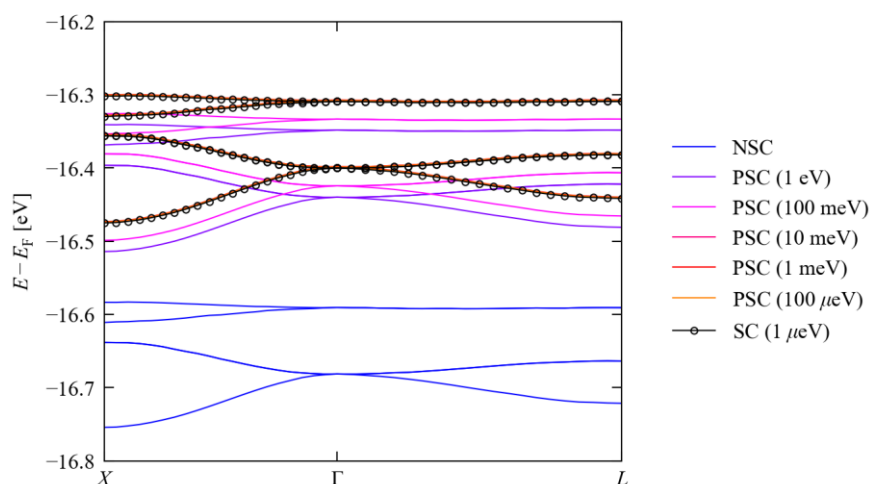


**Figure S7.9** Change in the dispersion of the semi-core In d bands in InSb calculated using non-self-consistent and partially-self-consistent HSE06 starting from the PBE orbitals with SCF convergence thresholds of 1 eV to 100  $\mu\text{eV}$  ( $10^0 - 10^{-4}$  eV). The black lines with markers show the reference dispersion obtained from fully self-consistent calculations performed to a tolerance of 1  $\mu\text{eV}$  ( $10^{-6}$  eV).

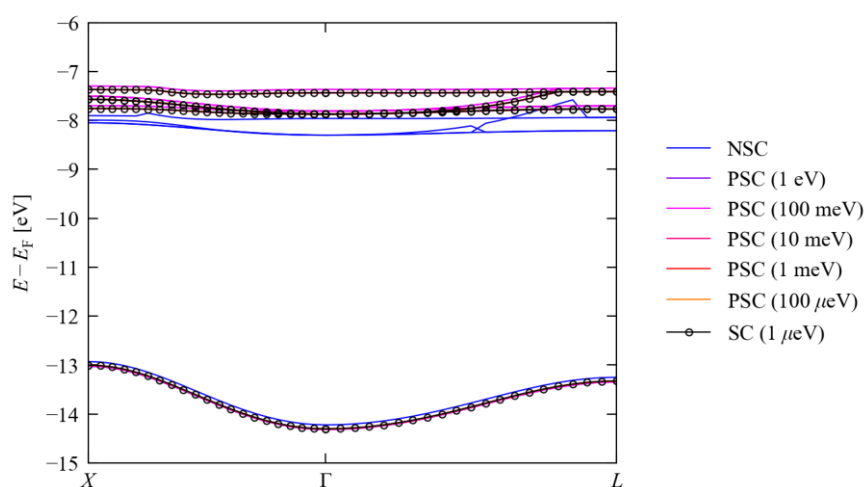


**Figure S7.10** Change in the dispersion of the Zn d bands in ZnS calculated using non-self-consistent and partially-self-consistent HSE06 starting from the PBE orbitals with SCF convergence thresholds of 1 eV to 100  $\mu\text{eV}$  ( $10^0 - 10^{-4}$  eV). The black lines with markers show the reference dispersion obtained from fully self-consistent calculations performed to a tolerance of 1  $\mu\text{eV}$  ( $10^{-6}$  eV).

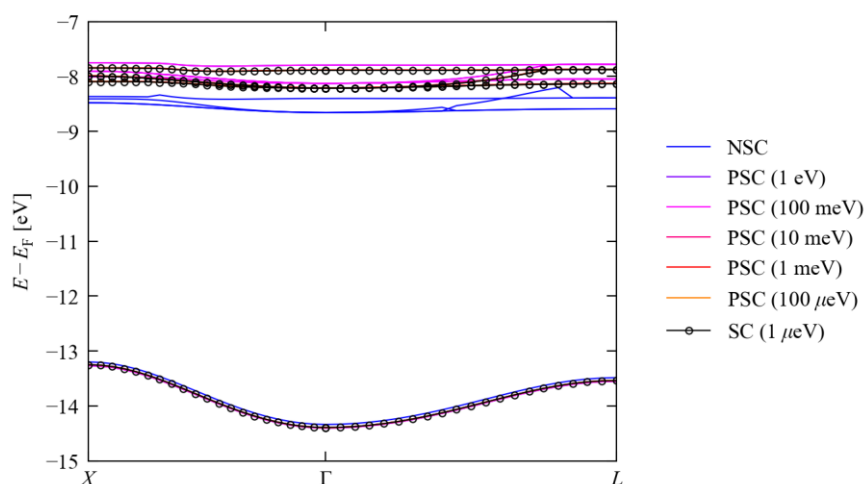


**Figure S7.11** Change in the dispersion of the Zn d bands in ZnSe calculated using non-self-consistent and partially-self-consistent HSE06 starting from the PBE orbitals with SCF convergence thresholds of 1 eV to 100  $\mu\text{eV}$  ( $10^0 - 10^{-4}$  eV). The black lines with markers show the reference dispersion obtained from fully self-consistent calculations performed to a tolerance of 1  $\mu\text{eV}$  ( $10^{-6}$  eV).

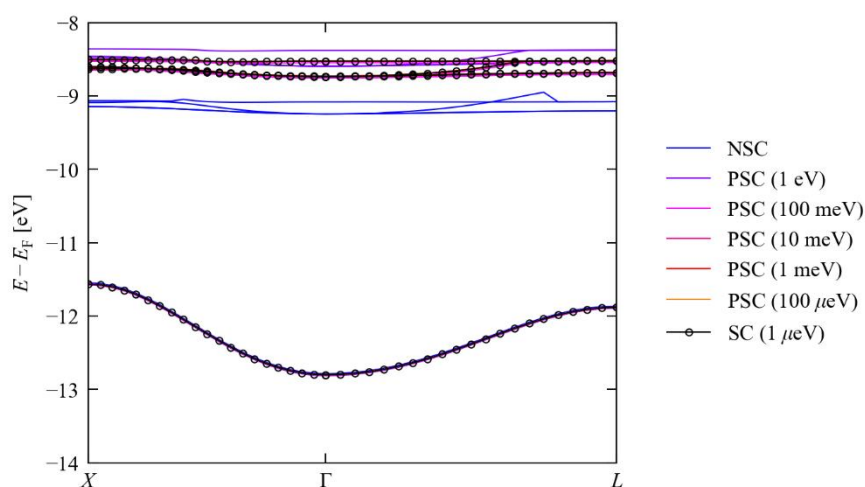


**Figure S7.12** Change in the dispersion of the Zn d bands in ZnTe calculated using non-self-consistent and partially-self-consistent HSE06 starting from the PBE orbitals with SCF convergence thresholds of 1 eV to 100  $\mu\text{eV}$  ( $10^0 - 10^{-4}$  eV). The black lines with markers show the reference dispersion obtained from fully self-consistent calculations performed to a tolerance of 1  $\mu\text{eV}$  ( $10^{-6}$  eV).

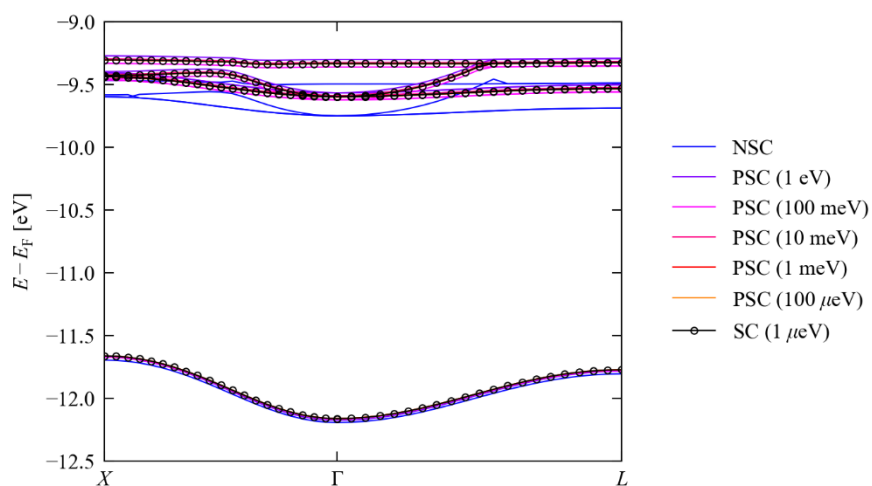


**Figure S7.13** Change in the dispersion of the Cd d bands in CdTe calculated using non-self-consistent and partially-self-consistent HSE06 starting from the PBE orbitals with SCF convergence thresholds of 1 eV to 100  $\mu\text{eV}$  ( $10^0 - 10^{-4}$  eV). The black lines with markers show the reference dispersion obtained from fully self-consistent calculations performed to a tolerance of 1  $\mu\text{eV}$  ( $10^{-6}$  eV).

## S8. Transition-Metal Oxides: CoO and NiO

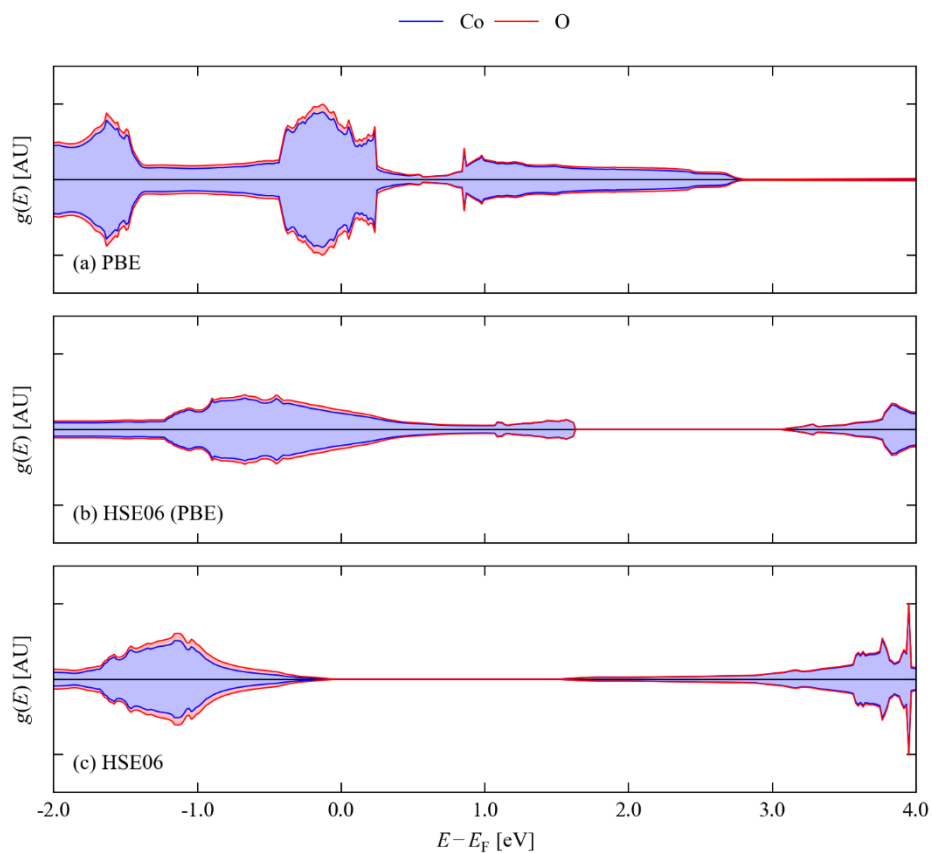


**Figure S8.1** Electronic density of states  $g(E)$  (DoS) of CoO calculated using PBE<sup>1</sup> (a), non-self-consistent HSE06<sup>9</sup> using the PBE orbitals (b) and self-consistent HSE06 (c). The DoS is drawn as a stacked-area plot showing the projection onto Co (blue) and O (red) atomic states.

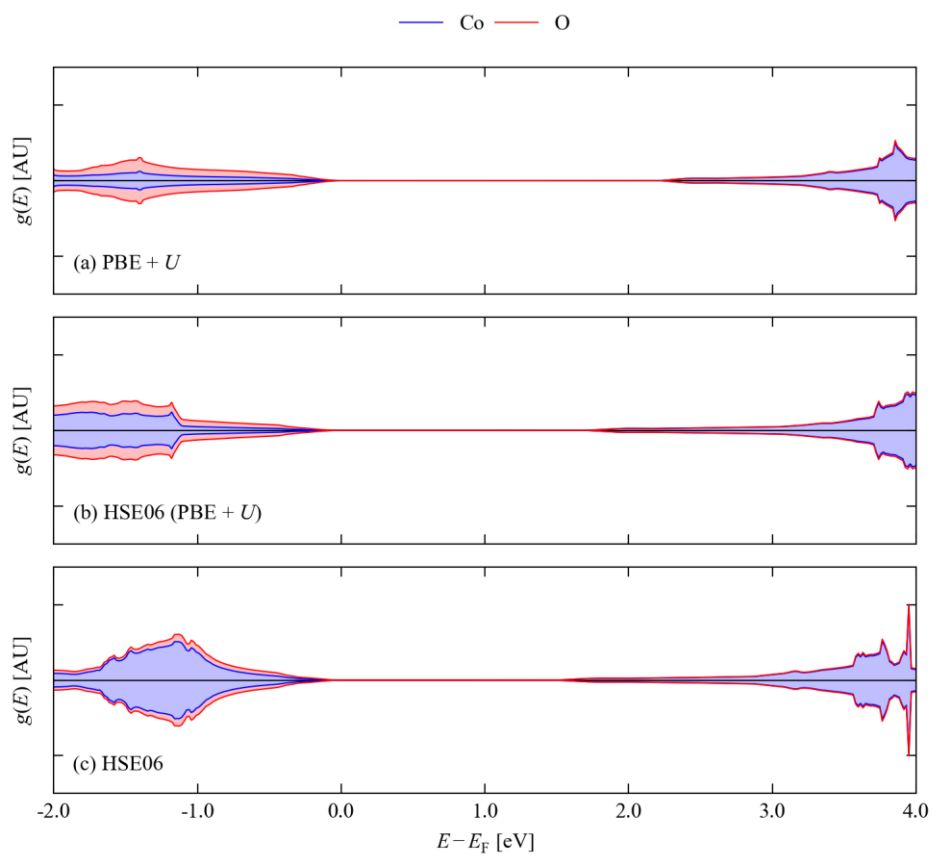


**Figure S8.2** Electronic density of states  $g(E)$  (DoS) of CoO calculated using PBE +  $U$  (a), non-self-consistent HSE06 using the PBE +  $U$  orbitals (b) and self-consistent HSE06 (c). Details of the PBE +  $U$  calculations are given in the text. The DoS is drawn as a stacked-area plot showing the projection onto Co (blue) and O (red) atomic states.

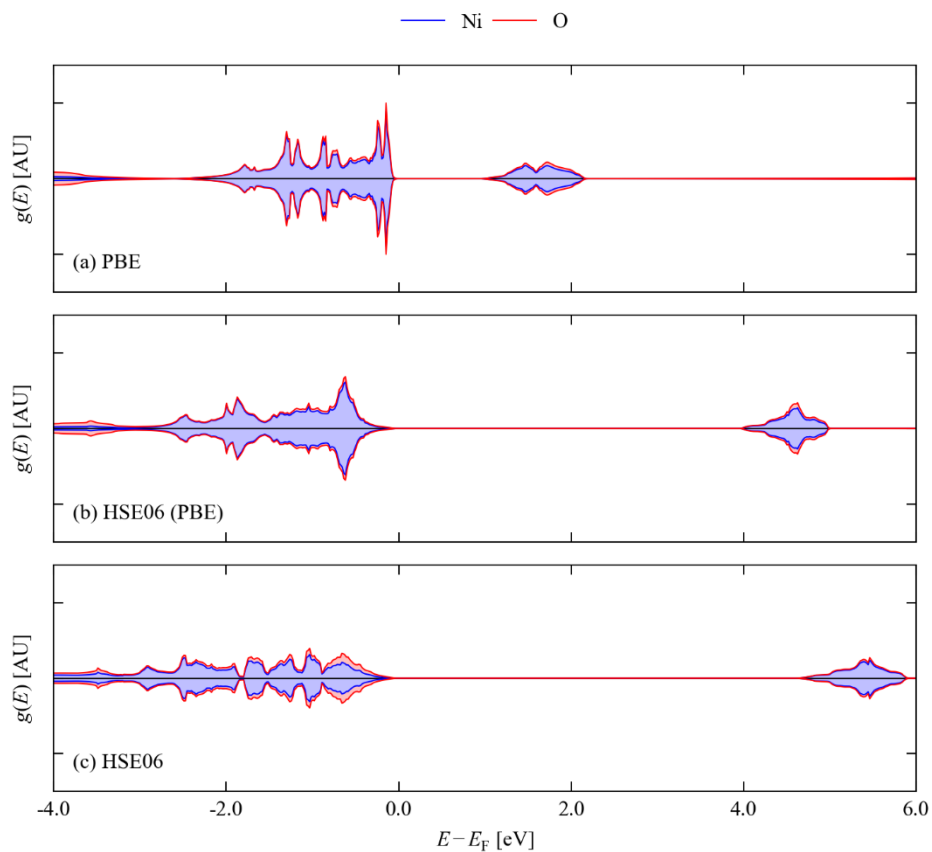


**Figure S8.3** Electronic density of states  $g(E)$  (DoS) of NiO calculated using PBE (a), non-self-consistent HSE06 using the PBE orbitals (b) and self-consistent HSE06 (c). The DoS is drawn as a stacked-area plot showing the projection onto Ni (blue) and O (red) atomic states.

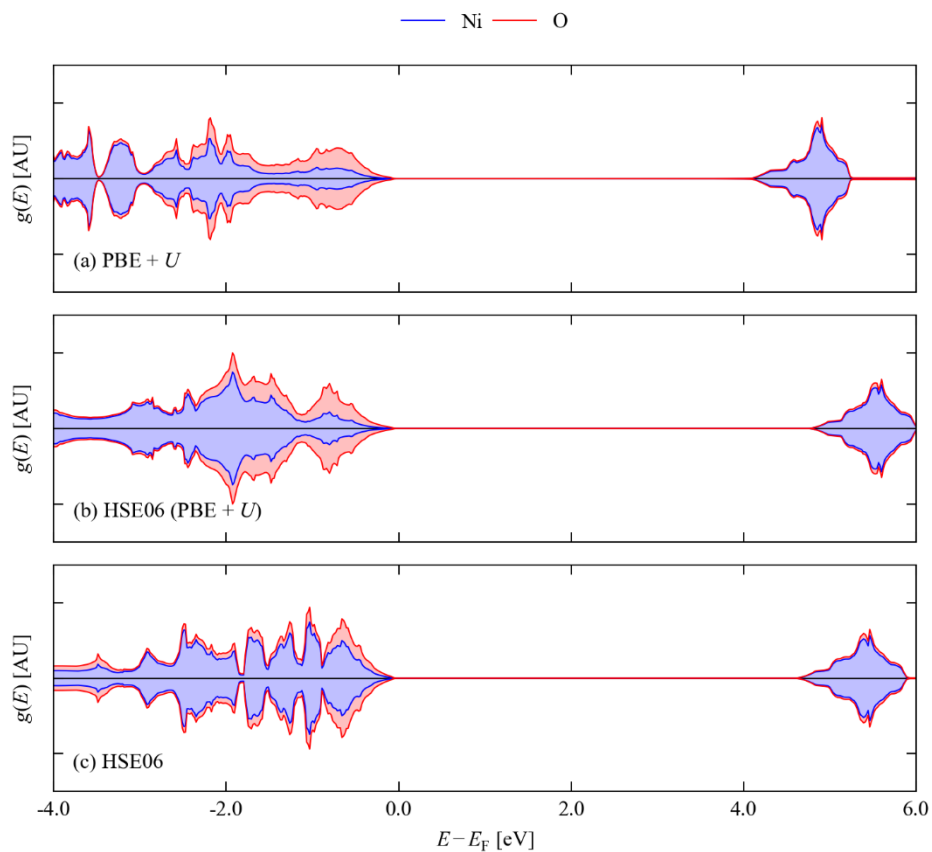


**Figure S8.4** Electronic density of states  $g(E)$  (DoS) of NiO calculated using PBE +  $U$  (a), non-self-consistent HSE06 using the PBE +  $U$  orbitals (b) and self-consistent HSE06 (c). Details of the PBE +  $U$  calculations are given in the text. The DoS is drawn as a stacked-area plot showing the projection onto Ni (blue) and O (red) atomic states.



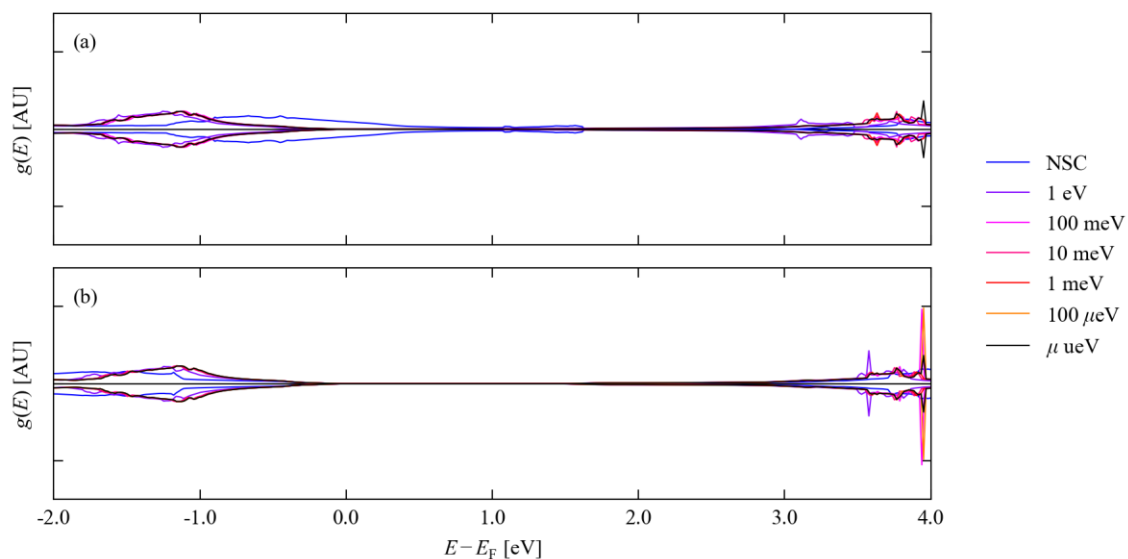


**Figure S8.5** Change in the valence band density of states  $g(E)$  (DoS) of CoO calculated using HSE06 starting from the PBE (a) and PBE +  $U$  orbitals (b) with SCF tolerances of 1 eV - 100  $\mu$ eV ( $10^0$ - $10^{-4}$  eV) on the total energy. Details of the PBE +  $U$  calculations are given in the text. The lines are colour coded from blue to orange to indicate successively tighter convergence thresholds. The blue line shows the DoS obtained from non-self-consistent calculations using the initial orbitals, and the black line shows the reference DoS obtained from the fully self-consistent calculation performed to a tolerance of 1  $\mu$ eV ( $10^{-6}$  eV).

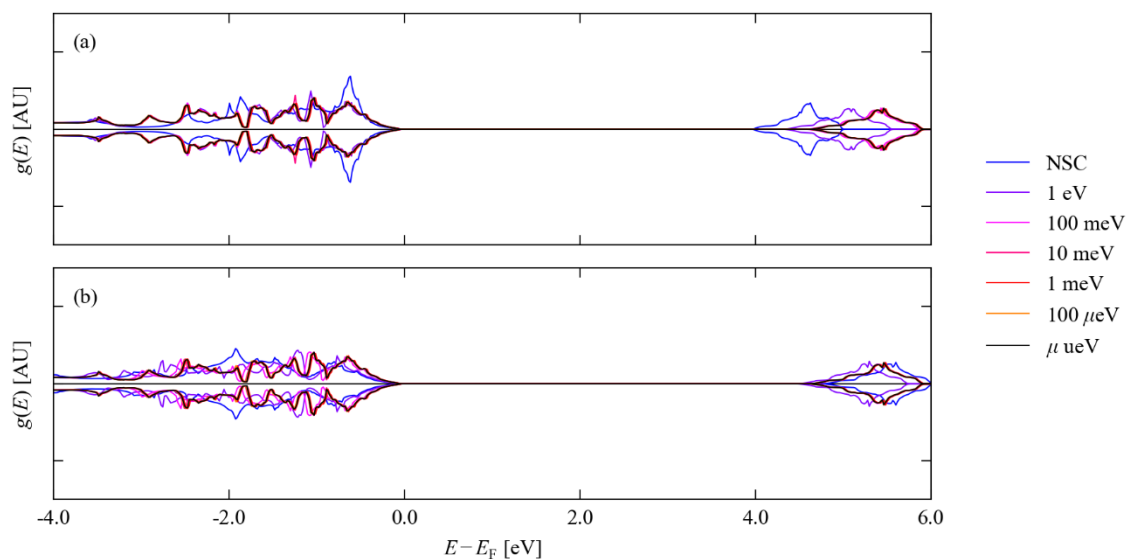


**Figure S8.6** Change in the valence band density of states  $g(E)$  (DoS) of NiO calculated using HSE06 starting from the PBE (a) and PBE +  $U$  orbitals (b) with SCF tolerances of 1 eV - 100  $\mu$ eV ( $10^0$ - $10^{-4}$  eV) on the total energy. Details of the PBE +  $U$  calculations are given in the text. The lines are colour coded from blue to orange to indicate successively tighter convergence thresholds. The blue line shows the DoS obtained from non-self-consistent calculations using the initial orbitals, and the black line shows the reference DoS obtained from the fully self-consistent calculation performed to a tolerance of 1  $\mu$ eV ( $10^{-6}$  eV).

## S9. References

- (1) Perdew, J. P.; Burke, K.; Ernzerhof, M. Generalized Gradient Approximation Made Simple. *Phys. Rev. Lett.* **1996**, *77*, 3865–3868.
- (2) Birch, F. Finite Elastic Strain of Cubic Crystals. *Phys. Rev.* **1947**, *71*, 809–824.
- (3) Gajdoš, M.; Hummer, K.; Kresse, G.; Furthmüller, J.; Bechstedt, F. Linear Optical Properties in the Projector-Augmented Wave Methodology. *Phys. Rev. B* **2006**, *73*, 045112.
- (4) Nunes, R. W.; Gonze, X. Berry-Phase Treatment of the Homogeneous Electric Field Perturbation in Insulators. *Phys. Rev. B* **2001**, *63*, 155107.
- (5) Hedin, L. New Method for Calculating the One-Particle Green's Function with Application to the Electron-Gas Problem. *Phys. Rev.* **1965**, *139*, A796–A823.
- (6) Salpeter, E. E.; Bethe, H. A. A Relativistic Equation for Bound-State Problems. *Phys. Rev.* **1951**, *84*, 1232–1242.
- (7) Sander, T.; Maggio, E.; Kresse, G. Beyond the Tamm-Dancoff Approximation for Extended Systems Using Exact Diagonalization. *Phys. Rev. B - Condens. Matter Mater. Phys.* **2015**, *92*, 045209.
- (8) Adamo, C.; Barone, V. Toward Reliable Density Functional Methods without Adjustable Parameters: The PBE0 Model. *J. Chem. Phys.* **1999**, *110*, 6158.
- (9) Krukau, A. V.; Vydrov, O. A.; Izmaylov, A. F.; Scuseria, G. E. Influence of the Exchange Screening Parameter on the Performance of Screened Hybrid Functionals. *J. Chem. Phys.* **2006**, *125*, 224106.
- (10) Souza, I.; Íñiguez, J.; Vanderbilt, D. First-Principles Approach to Insulators in Finite Electric Fields. *Phys. Rev. Lett.* **2002**, *89*, 117602.
- (11) Ceperley, D. M.; Alder, B. J. Ground State of the Electron Gas by a Stochastic Method. *Phys. Rev. Lett.* **1980**, *45*, 566–569.
- (12) Perdew, J. P.; Ruzsinszky, A.; Csonka, G. I.; Vydrov, O. A.; Scuseria, G. E.; Constantin, L. A.; Zhou, X.; Burke, K. Restoring the Density-Gradient Expansion for Exchange in Solids and Surfaces. *Phys. Rev. Lett.* **2008**, *100*, 136406.
- (13) Tao, J.; Perdew, J. P.; Staroverov, V. N.; Scuseria, G. E. Climbing the Density Functional Ladder: Nonempirical Meta-Generalized Gradient Approximation Designed for Molecules and Solids. *Phys. Rev. Lett.* **2003**, *91*, 146401.
- (14) Perdew, J. P.; Ruzsinszky, A.; Csonka, G. I.; Constantin, L. A.; Sun, J. Workhorse Semilocal Density

Functional for Condensed Matter Physics and Quantum Chemistry. *Phys. Rev. Lett.* **2009**, *103*, 026403.

- (15) Sun, J.; Ruzsinszky, A.; Perdew, J. P. Strongly Constrained and Appropriately Normed Semilocal Density Functional. *Phys. Rev. Lett.* **2015**, *115*, 036402.